

# The mechanism of YAP/TAZ transactivation and dual targeting for cancer therapy

Received: 26 June 2024

Accepted: 17 April 2025

Published online: 24 April 2025



Man Yu<sup>1,7</sup>, Jingning Wang<sup>2,7</sup>, Xiao Zhang<sup>1</sup>, Haoran Zhang<sup>2</sup>, Chaoqiang Li<sup>3</sup>,  
Juebei Li<sup>1</sup>, Jiaming Lin<sup>1</sup>, Jie Zheng<sup>3,4</sup>, Liu Huang<sup>5</sup>, Yan Li<sup>2,6</sup> ✉ &  
Shuguo Sun<sup>1</sup> ✉

Transcriptional coactivators Yes-associated protein (YAP) and transcriptional coactivator with PDZ-binding motif (TAZ) play key roles in cancers through transcriptional outputs. However, their transactivation mechanisms remain unclear, and effective targeting strategies are lacking. Here, we show that YAP/TAZ possess a hydrophobic transactivation domain (TAD). TAD knockout prevents tumor establishment due to growth defects and enhances immune attack. Mechanistically, TADs facilitate preinitiation complex (PIC) assembly by recruiting the TATA-binding protein-associated factor 4 (TAF4)-dependent TFIID complex and enhance RNA polymerase II (Pol II) elongation through mediator complex subunit 15 (MED15)-dependent mediator recruitment for the expressions of oncogenic/immune-suppressive programs. The synthesized peptide TJ-M11 selectively disrupts TAD interactions with MED15 and TAF4, suppressing tumor growth and sensitizing tumors to immunotherapy. Our findings demonstrate that YAP/TAZ TADs exhibit dual functions in PIC assembly and Pol II elongation via hydrophobic interactions, which represent actionable targets for cancer therapy and combination immunotherapy.

YAP/TAZ, a pair of paralogs of potent transcriptional coactivators, function downstream of the Hippo pathway in cancer initiation, progression, and immunotherapy resistance by promoting the transcription of target genes transcription<sup>1–7</sup>. Compared to their functions in covalent and noncovalent epigenetic regulation<sup>8–11</sup>, the mechanism and in vivo function of YAP/TAZ to initiate transcription is not well known. Like other transcription events, the specific binding of YAP/TAZ to DNA through TEA domain (TEAD) family transcription factors (TFs) has been well documented, whereas how their intrinsically disordered regions (IDRs) of TAD promoting transactivation has been unresolved questions<sup>12</sup>. There are over 2000 TFs with hundreds of TADs in human genome<sup>13,14</sup> and these TADs exhibited obvious primary

sequences variation and functional conservation through interacting with only a few cofactors for driving transcription. The mechanism underlying TAD and cofactors interactions driving transcriptions needs to be addressed<sup>15</sup>. Thus, dissecting the structure and function of YAP/TAZ-TADs will facilitate the understanding of the transcription output of YAP/TAZ as well as provide potential targeting strategies.

YAP/TAZ are upregulated in numerous human cancers and exhibit strong multipotency in autonomous tumor cell growth, non-autonomous immune suppression, microenvironment regulation, and immunotherapy resistance<sup>1,6,16</sup>. Because of the key function of YAP/TAZ in solid tumors, targeting them for clinical applications is striking<sup>17</sup>. Previous studies have focused mainly on the interaction

<sup>1</sup>Department of Human Anatomy, Histology and Embryology, School of Basic Medicine, Tongji Medical College and State Key Laboratory for Diagnosis and Treatment of Severe Zoonotic Infectious Diseases, Huazhong University of Science and Technology, Wuhan, China. <sup>2</sup>Department of Pathogen Biology, School of Basic Medicine, Tongji Medical College and State Key Laboratory for Diagnosis and Treatment of Severe Zoonotic Infectious Diseases, Huazhong University of Science and Technology, Wuhan, China. <sup>3</sup>Shanghai Institute of Materia Medica, Chinese Academy of Sciences, Shanghai, China. <sup>4</sup>School of Pharmaceutical Science and Technology, Hangzhou Institute for Advanced Study, UCAS, Hangzhou, China. <sup>5</sup>Department of Oncology, Tongji Hospital, Tongji Medical College, Huazhong University of Science and Technology, Wuhan, China. <sup>6</sup>Hubei Key Laboratory of Drug Target Research and Pharmacodynamic Evaluation, Wuhan, China. <sup>7</sup>These authors contributed equally: Man Yu, Jingning Wang. ✉e-mail: [yanli@hust.edu.cn](mailto:yanli@hust.edu.cn); [shuguo@hust.edu.cn](mailto:shuguo@hust.edu.cn)

between TEAD and YAP<sup>18</sup>. Several strategies have been developed to identify small molecules and peptides that block TEAD-YAP interactions<sup>19,20</sup>. However, to date, no drugs that inhibit YAP have been clinically used because of their limited activity or cytotoxicity. The prevention of transcriptional activation by small peptides or chemicals has recently shown good efficacy against some key onco-transcription factors<sup>21,22</sup>. Thus, targeting the interactions between intrinsically disordered TFs and cofactors is a potential field for drug development. However, challenges remain due to the dynamic interface of these interactions<sup>23</sup>.

Here, we show the structure and function of YAP and TAZ transactivation domains. They exhibit dual functions during transcriptional activation including initiation and elongation. TADs assemble the pre-initiation complex for Pol II loading by interacting with TAF4 and promote Pol II efficient elongations via recruiting the mediator complex. Both TFIID and the Mediator complex bind to transcriptional activation domains (TADs) through hydrophobic interactions involving an  $\alpha$ -helix and the linear FLTWL motif. This interaction promotes the folding of the IDR, facilitating the formation of transcriptional condensates via co-condensation. Knockout of TADs of YAP/TAZ leads to tumor growth defects and enhances immune response due to reducing oncogenic and immunosuppressive transcriptional program expression. Dual targeting of the interaction between the TADs of YAP/TAZ and the cofactors TAF4 and MED15 by small peptides mimicking FLTWL inhibits their transactivation activity. This suppresses tumor growth and enhances the efficacy of immunotherapy, supporting the strategy of targeting the transactivation domains of YAP/TAZ for cancer therapy.

## Results

### Structural characterization of TADs of YAP and TAZ

Our previous studies identified a 55-amino acid TAD at the C-terminus of YAP<sup>24</sup>. To determine whether TAZ has a similar TAD, we performed protein sequence alignments and evaluated their activities using Gal4-UAS-luciferase reporter assays (Fig. 1a). Similarly, the final 35 residues (366–400) at the C-terminus of TAZ could initiate reporter gene transcription, although with only one-third of the activity seen in YAP-TAD (Fig. 1b). Notably, both TADs were composed of over 50% hydrophobic and ~20% acidic amino acids (Fig. 1c). Interestingly, at the termini of these TADs is a five-residue linear hydrophobic motif FLTWL, previously identified as the PDZ binding domain<sup>25</sup>. Hydrophilic replacement with four serine residues (S) disrupted the ability to drive the transcription of cellular target genes (Fig. 1d).

To dissect the structures of both TADs, we performed nuclear magnetic resonance (NMR) analysis (Fig. 1e, f) on highly purified protein samples expressed and purified from *E. coli* (Supplementary Fig. 1a, b). The solution structure of YAP-TAD has been resolved and submitted to Protein Data Bank (PDB) under accession number 8WRG. Our results revealed that the TADs were predominantly composed of IDRs (Fig. 1e, f and Supplementary Fig. 1c–f). Compared to the TAD of TAZ, the TAD of YAP exhibited a short amphipathic  $\alpha$ -helix spanning seven amino acids, with AlphaFold2 predictions suggesting a potential extension of up to 17 residues (Fig. 1g). Interestingly, substituting residues asparagine (N) and serine (S) on the hydrophilic surface with hydrophobic residue leucine (L) enhanced transcriptional activation. Conversely, replacing hydrophobic residues on the hydrophobic surface with serine (S) reduced transcriptional activity (Fig. 1h and Supplementary Fig. 1g). These results indicate that YAP possesses a hydrophobic TAD, and the interactions between the amphipathic helix and the FLTWL motif with TFs are crucial for YAP over-expression induced gene activation.

### The TAD of YAP initiates immunosuppressive transcriptional program

Next, we evaluated the functional significance of TADs of YAP/TAZ in transcriptional promotion and tumor growth using a *Kras*<sup>LSL;G12D</sup>; *Trp53*<sup>fl</sup>

mouse lung tumor-derived cell line (TDCL)<sup>26</sup> (Supplementary Fig. 2a). To this end, we knocked out the TAD of YAP in *TAZ*<sup>-/-</sup> background by generating a frameshift near the start residue of the TAD of YAP using the clustered regularly interspaced short palindromic repeats (CRISPR-Cas9) assay (Supplementary Fig. 2b). The loss of TAD or FLTWL in YAP did not affect its stability or nuclear localization (Supplementary Fig. 2c, d). To test whether TADs are essential for tumor cell growth, we examined the growth of TDCL with TADs depletion using plate cloning and allograft assays in C57BL/6J mice. The results showed that knockout of TADs partially impaired tumor cell growth in vitro (Supplementary Fig. 2e). Strikingly, tumors with TAD depletion could not be established in immune-competent animals (Supplementary Fig. 2f), suggesting a strong immune attack from the hosts when TADs are depleted.

To evaluate the contribution of TADs of YAP/TAZ in immunosuppression, we transplanted tumors with TADs depletion in immunodeficient NCG (NOD/ShiLtJGpt-*Prkdc*<sup>em26Cd52</sup>*Il2rg*<sup>em26Cd22</sup>/Gpt) mice and compared their growth in C57BL/6J mice. Obviously, the tumors in immunodeficient mice can grow bigger than those in C57BL/6J mice (Fig. 2a). To assess tumor-specific immune responses, we examined CD8<sup>+</sup> T cells specific to ovalbumin (OVA) using H-2K(b) OVA tetramer antibodies. Initially, we transfected wild-type or TAD-deficient TDCL cells with a lentiviral vector expressing OVA fused with nano-luciferase (nLuc). Comparable intracellular luciferase activity confirmed similar OVA expression levels between the two cell lines (Supplementary Fig. 2g). Subsequently, we subcutaneously implanted these cells into C57BL/6J mice. Our results demonstrated that tumors lacking TAD exhibited increased infiltration of OVA-tetramer-positive CD8<sup>+</sup> T cells (Fig. 2b, c). Moreover, infiltrating CD8<sup>+</sup> T cells from TAD-depleted tumors displayed higher fraction and enhanced cytotoxic activity (Fig. 2d, e and Supplementary Fig. 2h), suggesting a role for YAP-TAD in mediating immunosuppression within the tumor microenvironment. Importantly, depletion of CD8<sup>+</sup> T cells using anti-CD8 antibody in C57BL/6 mice restored tumor growth in TAD-depleted tumors (Supplementary Fig. 2i, j). To exclude potential effects of Cas9 neoantigens, we restored YAP expression in TAD-deficient cells. Our results showed that restorage of YAP expression reversed both the tumor growth defects and target gene downregulations due to TAD deficiency (Supplementary Fig. 2j, k). Collectively, these findings highlight the critical role of CD8<sup>+</sup> T cell-mediated antitumor immunity in the context of TAD deficiency.

To identify YAP-TAD target genes involved in immunosuppression, we performed RNA sequencing followed by Gene Set Enrichment Analysis (GSEA). Our results showed significant downregulation of classic YAP/TAZ target genes, highlighting the essential role of YAP-TAD in transcriptional regulation (Fig. 2f). Additionally, we identified reduced expression of both known and novel immunosuppressive genes, including *Tgfb2*, *Il33*, and *Itgb2*, which play key roles in immunosuppression (Fig. 2g, Supplementary Fig. 2l).

To validate these genes as direct YAP-TAD targets, we conducted RT-qPCR in TAD-depleted and WT cells, confirming their reduced expression upon TAD depletion (Fig. 2h, Supplementary Fig. 2m). Notably, *Csf1* and *Il33* are known to promote macrophage recruitment and M2 polarization, contributing to tumor immunosuppression<sup>27–29</sup>. Immunofluorescence (IF) staining for CD206 and CD163 further revealed that YAP-TAD depletion significantly decreased M2 macrophage infiltration, which in turn enhanced CD8<sup>+</sup> T cell infiltration and cytotoxicity (Fig. 2e).

In summary, our findings demonstrate that the TADs of YAP/TAZ are essential for driving oncogenic and immunosuppressive transcriptional programs in tumorigenesis.

### TADs of YAP/TAZ initiate PIC assembly and Pol II loading through recruiting TAF4

To explore the detail molecular mechanism underlying transcriptional activation by the TADs of YAP/TAZ, we first performed the spatial

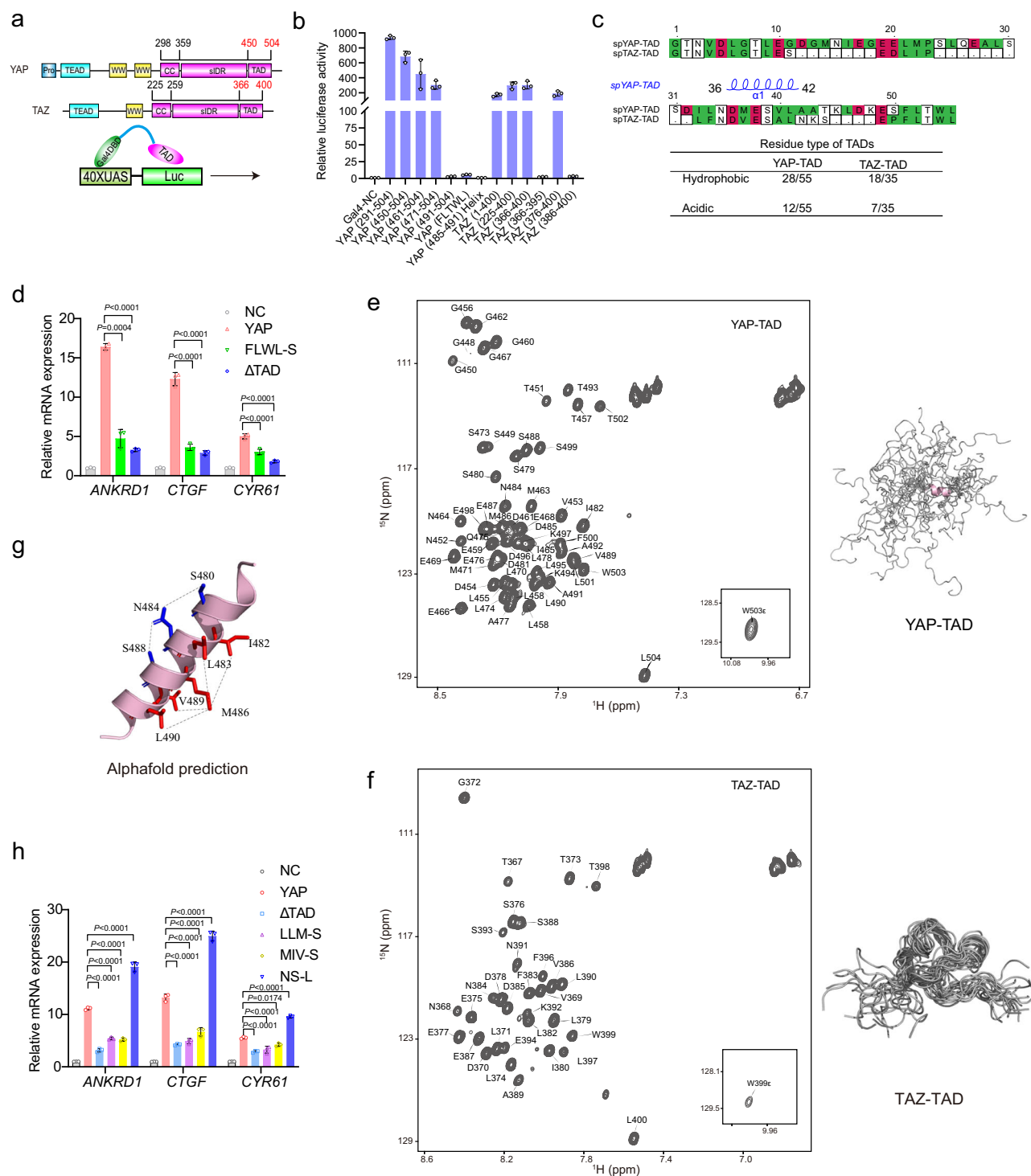


**Fig. 1 | Structural characterization of TADs of YAP and TAZ. a** Diagram of the conserved domains of YAP/TAZ and the Gal4-UAS-Luciferase reporter system for the TAD activity test. (Pro: Proline, CC: Coiled coil domain, WW: WW domain, siDR: small Intrinsic Disorder Region. TAD: Transactivation Domain, 40×UAS: 40 repeats of Upstream Activating Sequence). **b** Luciferase activity of HEK293T cells co-transfected with the indicated plasmids and 40× UAS-luciferase reporters ( $n = 3$  biological replicates). **c** Sequence alignment of YAP and TAZ TADs. Acidic amino acids are shown in red, and hydrophobic amino acids are shown in green. **d** RT-qPCR shows YAP target genes in HEK293T cell transfected with YAP, YAP $\Delta$ TAD, or F500L501W503L504 mutating to S ( $n = 3$  biological replicates). **e** Assignments of

backbone amide groups of YAP-TAD and NMR structure ensemble of YAP-TAD consisting of the 20 lowest-energy models. The  $\alpha$ -helix is shown in pink and the intrinsically disordered region in gray. **f** Assignments of backbone amide groups of TAZ-TAD and NMR structure ensemble of TAZ-TAD consisting of the 20 lowest-energy models. **g** Predicted structural model of the  $\alpha$ -helix of YAP-TAD by AlphaFold2. Hydrophilic (blue) and hydrophobic (red) residues are indicated. **h** RT-qPCR analysis of YAP target genes in HEK293T cells transfected with YAP, YAP $\Delta$ TAD, L483M486L490 to S, L482M486V489 to S, or N484S488 to L ( $n = 3$  biological replicates). Data are presented as mean  $\pm$  standard error of the mean (SEM). Statistical analyses were performed using one-way ANOVA (**d**, **h**).

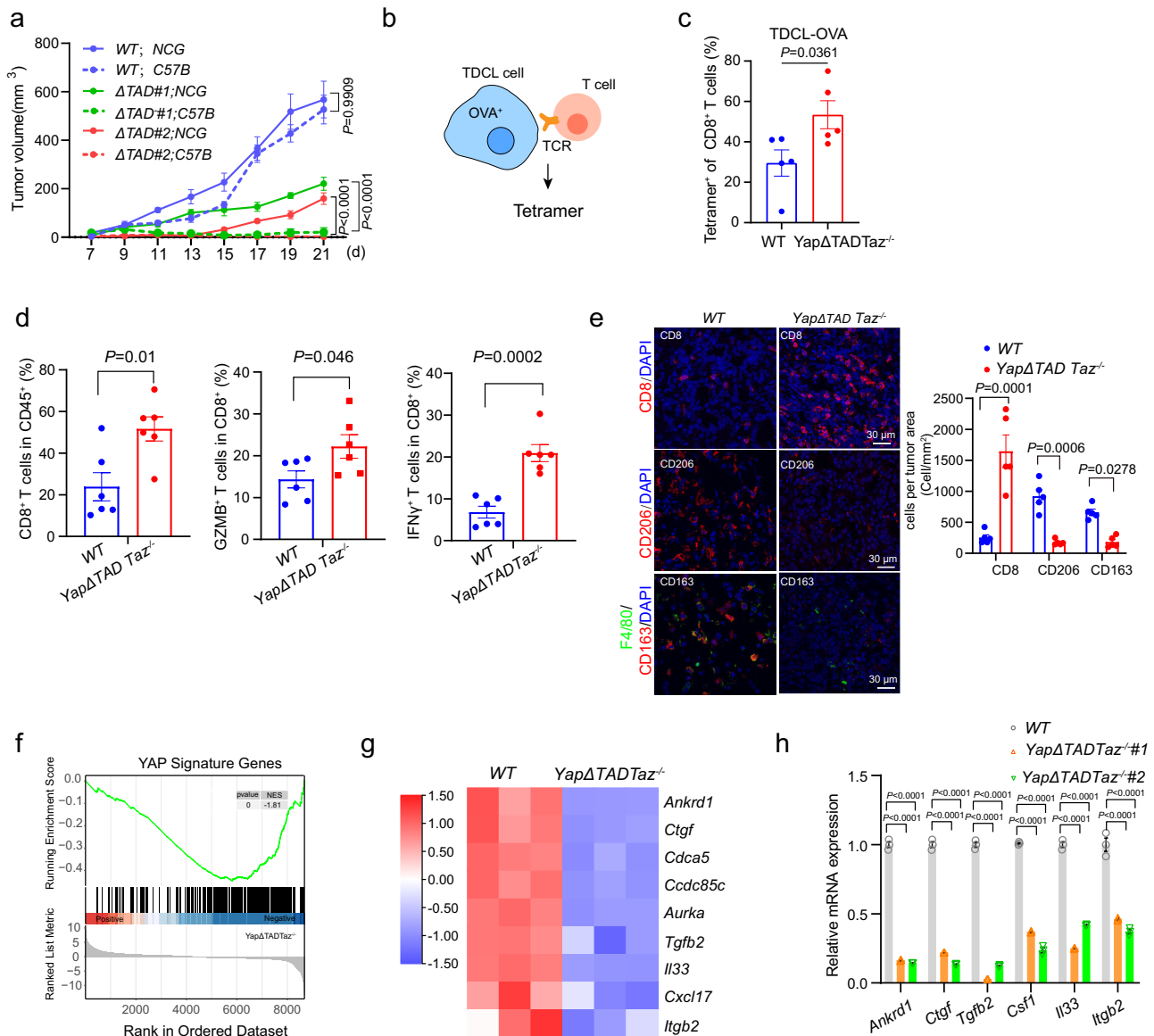


**Fig. 2 | The TAD of YAP initiates immunosuppressive transcriptional program.**

**a** Tumor growth of TDCL WT, *YapΔTAD Taz<sup>-/-</sup>* #1, and *YapΔTAD Taz<sup>-/-</sup>* #2 cells injected subcutaneously to C57BL/6J mice or NCG mice ( $n = 5$  mice per group). **b** Tetramer experimental design of tumor-specific T cells against OVA<sup>+</sup> cancer cells. **c** Flow cytometry analysis of OVA-tetramer<sup>+</sup> in CD8<sup>+</sup> T cells of TDCL WT-OVA, *YapΔTAD Taz<sup>-/-</sup>* OVA tumors in C57BL/6J mice ( $n = 5$  mice per group). **d** Flow cytometry analysis of CD8<sup>+</sup> T cells in CD45<sup>+</sup> cells, GZMB<sup>+</sup> cells, and IFN- $\gamma$ <sup>+</sup> cells of TDCL WT, *YapΔTAD Taz<sup>-/-</sup>* tumors in C57BL/6J mice ( $n = 6$  mice per group). **e** Immunofluorescence images of TDCL WT, *YapΔTAD Taz<sup>-/-</sup>* tumors were stained

for CD8 (red), and macrophage markers CD206 (red), CD163 (red) and F4/80 (green). The value was calculated by counting total CD8<sup>+</sup>, CD206<sup>+</sup>, or CD163<sup>+</sup> cells / tumor area ( $n = 5$  per group). **f** GSEA analysis of YAP signature genes from RNA-seq data of TDCL *YapΔTAD Taz<sup>-/-</sup>* and WT Cells. YAP signature genes set was obtained from the Molecular Signatures Database (MsigDB). **g** Heatmap showed the YAP target genes and immune suppressive genes from RNA-seq. **h** RT-qPCR analysis of gene expression in indicated genotypes of TDCL cells ( $n = 3$  biological replicates). Data are presented as mean  $\pm$  SEM. Statistical analysis was performed using two-way ANOVA (**a**), 2-tailed Student's *t* test (**c–e**), one-way ANOVA (**h**).

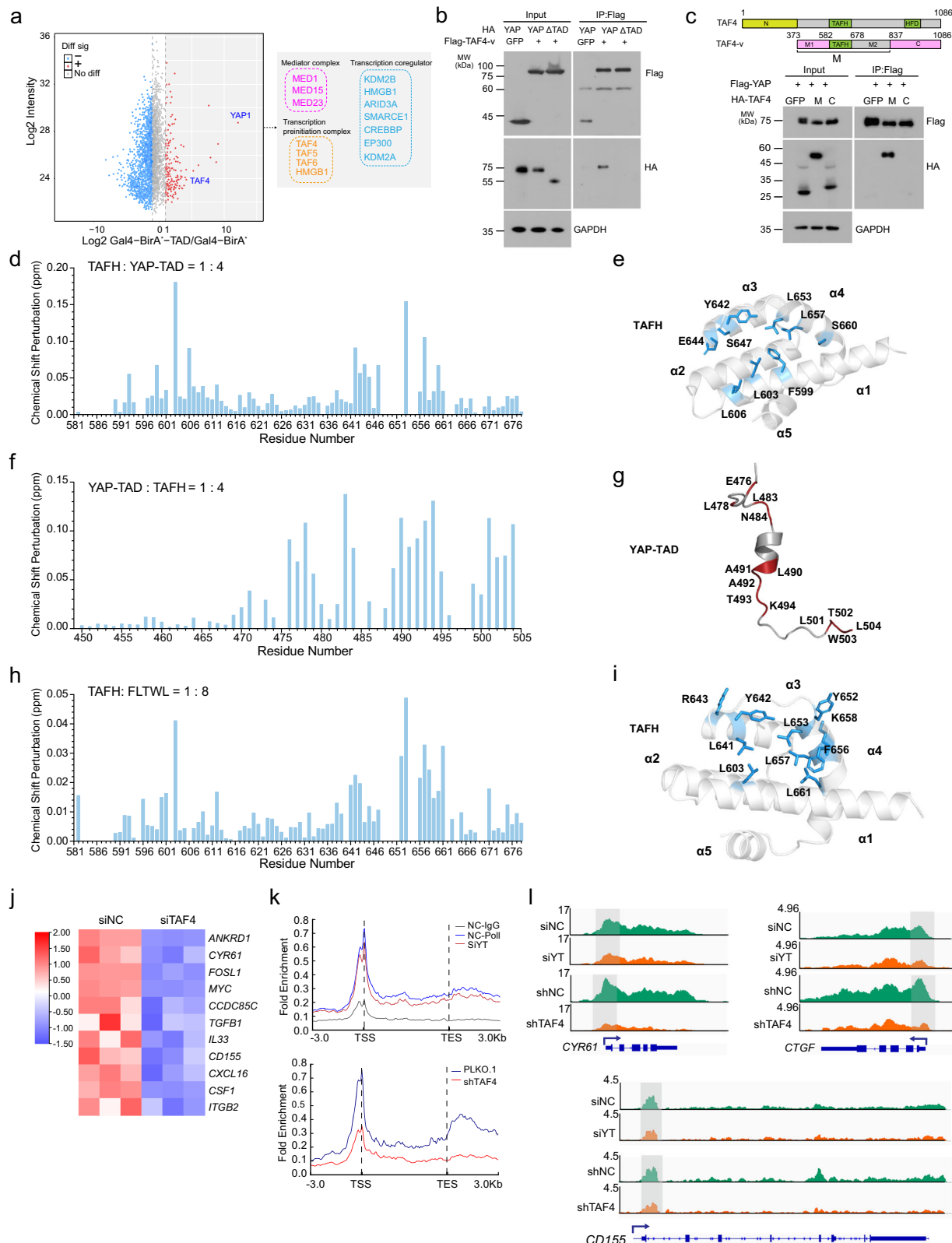
interactome of YAP TAD using a Proximity-dependent Biotin Identification assay (BioID) (Supplementary Fig. 3a). Enrichment analysis of the mass spectrometry profile identified several transcriptional components, including TFIID, the Mediator complex, and transcription coactivators (Fig. 3a and Supplementary Fig. 3b), suggesting the involvement of TADs in transcription initiation via interactions with these transcriptional cofactors.

To further confirm these interactions, we initially performed co-immunoprecipitation (Co-IP) assays to investigate the interactions between YAP and members of the TFIID family, which scored highly in the BioID assay and are key regulators of promoter occupancy. Our results showed that YAP physically interacts with TAF4 but not with TAF6, TAF7, or TAF9a

(Supplementary Fig. 3c, d). Notably, depletion of the TAD of YAP or FLTTL motif significantly weakened these interactions (Fig. 3b and Supplementary Fig. 3e). Similarly, depletion the TAD of TAZ reduced its interaction with TAF4 (Supplementary Fig. 3f), aligning with previous transcriptional activity analysis (Fig. 1d). Further Co-IP mapping revealed that the middle portion of TAF4 is crucial for interacting with YAP (Fig. 3c).

Prompted by the direct interactions observed in cells between the TAD of YAP and the middle fragment of TAF4, we employed NMR techniques to gain a more comprehensive and refined understanding of the binding interface between the two proteins. By dissecting the middle part of TAF4 into M1 (residues 373–582), M2 (residues 679–837), and the highly conserved TAF4 homology (TAFH) domain (residues





582–678)<sup>30</sup> (Fig. 3c), we expressed and purified the recombinant TAF4 M1, TAFH, M2, and TAF4<sub>582-837</sub> (i.e., TAFH + M2) proteins (Supplementary Fig. 3g–j) for biophysical characterization. Follow-up NMR titration assays revealed that TAF4 M1 and M2 were not observed to significantly interact with YAP-TAD (Supplementary Fig. 4a, c), but the binding affinity between TAF4<sub>582-837</sub> and YAP-TAD is similar to that of TAFH and YAP-TAD (Supplementary Fig. 4b and Supplementary

Fig. 5a), which narrowed the binding site of TAF4 to the TAFH domain. We subsequently obtained most of the backbone resonance assignments for TAFH, enabling further biophysical characterization. The <sup>1</sup>H-<sup>15</sup>N-HSQC spectrum for TAFH exhibits heterogeneously distributed peak intensities, resulting in the inability to assign the backbone resonances for certain residues in α1 (Supplementary Fig. 5b). These observations, possibly caused by severe peak broadening, reflect the

**Fig. 3 | TADs of YAP/TAZ initiate PIC assembly and Pol II loading through recruiting TAF4.** **a** BirA<sup>+</sup>-Gal4 and BirA<sup>+</sup>-Gal4-YAP-TAD were expressed with 40×UAS in HEK293T cells, and the cell lysates were subjected to BioID-MS. **b** HA-YAP or YAPΔTAD was co-expressed with Flag-TAF4-v and subjected to coimmunoprecipitation assay ( $n = 3$  independent experiments) (TAF4-v: TAF4 splice variant). **c** Flag-YAP was co-expressed with HA-TAF4 M<sub>373-837</sub> or HA-TAF4 C<sub>837-1086</sub> and subjected to coimmunoprecipitation assay ( $n = 3$  independent experiments). **d** Analysis for the CSP in <sup>1</sup>H-<sup>15</sup>N-HSQC of <sup>15</sup>N-TAFH upon titration with YAP-TAD. For **(d, f)**, CSP represents the difference in chemical shift of the peak position before and after titration. The detailed calculation method can be found in the Methods section. **e** The residues with significant CSP in **(d)** are mapped on the AlphaFold-predicted TAFH structure. **f** Analysis for CSP in <sup>1</sup>H-<sup>15</sup>N-HSQC of <sup>15</sup>N-labeled YAP-TAD upon titrations with TAFH. **g** The residues with significant CSP in **(f)** are mapped on

the YAP-TAD structure (red). **h** The CSP analysis for NMR titration of <sup>15</sup>N-TAFH with the pentapeptide FLTWL. **i** The residues with significant CSP in **(h)** are mapped on the AlphaFold-predicted TAFH structure (blue). **j** A heatmap of YAP target genes and immunosuppressive genes in NCI-H1299 siNC or siTAF4 cells, derived from RNA-seq. **k** Upper panel: YAP/TAZ siRNA CUT&Tag analysis Pol II occupancy of YAP target genes ( $n = 269$ ) in NCI-H1299 cells transfected with siNC or siYAP/TAZ (siYT). Lower panel: Metagene analysis showing total Pol II occupancy of YAP target genes ( $n = 242$ ) in NCI-H1299 PLKO.1 or shTAF4 cells (TSS transcription start sites, TES transcription end sites). **l** Representative genome browser tracks of Pol II CUT&Tag in NCI-H1299 siYT or shTAF4 cells for YAP target genes. The x-axis indicates the chromosome position, and the y-axis represents normalized read density in reads per million.

masked conformational dynamics of the putative hydrophobic pocket enclosed by these residues.

Based on the backbone assignments for TAFH, we investigated the binding interface of TAFH involved in the YAP-TAD and TAFH interactions using NMR titration experiments. Observations from the overlaid <sup>1</sup>H-<sup>15</sup>N-HSQC spectra of <sup>15</sup>N-TAFH in the presence or absence of YAP-TAD showed that peaks of certain TAFH residues experienced chemical shift perturbations (CSPs) upon YAP-TAD binding (Fig. 3d, e, and Supplementary Fig. 6a), indicating near μM-level binding affinity. These residues especially hydrophobic residues like L603, L653, L657, Y642, L606, and F599, were primarily scattered around the α1/α3/α4 helices, enclosing a hydrophobic pocket (Fig. 3e). The structural model of TAFH was predicted by AlphaFold2. In a reverse series of NMR titration assays, in which <sup>15</sup>N-labeled YAP-TAD was titrated with TAFH, both the C-terminal FLTWL motif and part of the helix of YAP-TAD displayed major chemical shift perturbations, indicating their deep involvement in TAD-TAFH interactions (Fig. 3f, g). Notably, the results of the two titrations indicated the involvement of the hydrophobic regions in both YAP-TAD and TAFH. Considering the similarity in hydrophobicity between the helix and the FLTWL of YAP-TAD, we conducted two additional NMR titration experiments to examine the binding properties of the standalone peptide fragments of these two regions toward TAFH. Interestingly, we observed that both fragments bound to almost the same hydrophobic pocket of TAFH as full-length YAP-TAD (Fig. 3h, i and Supplementary Fig. 6b, c). Collectively, NMR analysis revealed that the YAP-TAF4 interaction was heavily dependent on hydrophobic interactions, specifically involving a hydrophobic pocket on TAFH domain of TAF4 and both the α-helical region and FLTWL motif on YAP-TAD.

To further investigate the functional implications of the protein–protein interaction (PPI) between TAF4 and YAP-TAD in YAP-driven transcription, we measured the mRNA levels of target genes by RT-qPCR following TAF4 knockdown, both with and without YAP overexpression. TAF4 knockdown consistently reduced the classic target genes (*CTGF*, *CYR61*, and *ANKRD1*) expression in both conditions (Supplementary Fig. 7a, b). Moreover, overexpression of YAP did not reverse the reduction in YAP target gene expression by TAF4 knockdown (Supplementary Fig. 7c). To assess the broader impact of TAF4 on YAP/TAZ genome-wide transcriptional activity, we conducted transcriptome profiling and observed the downregulation of YAP typical target genes *ANKRD1*, *CYR61*, *MYC* and the immunosuppressive genes *CSF1*, *IL33*, and *ITGB2*. (Fig. 3j and Supplementary Fig. 7d).

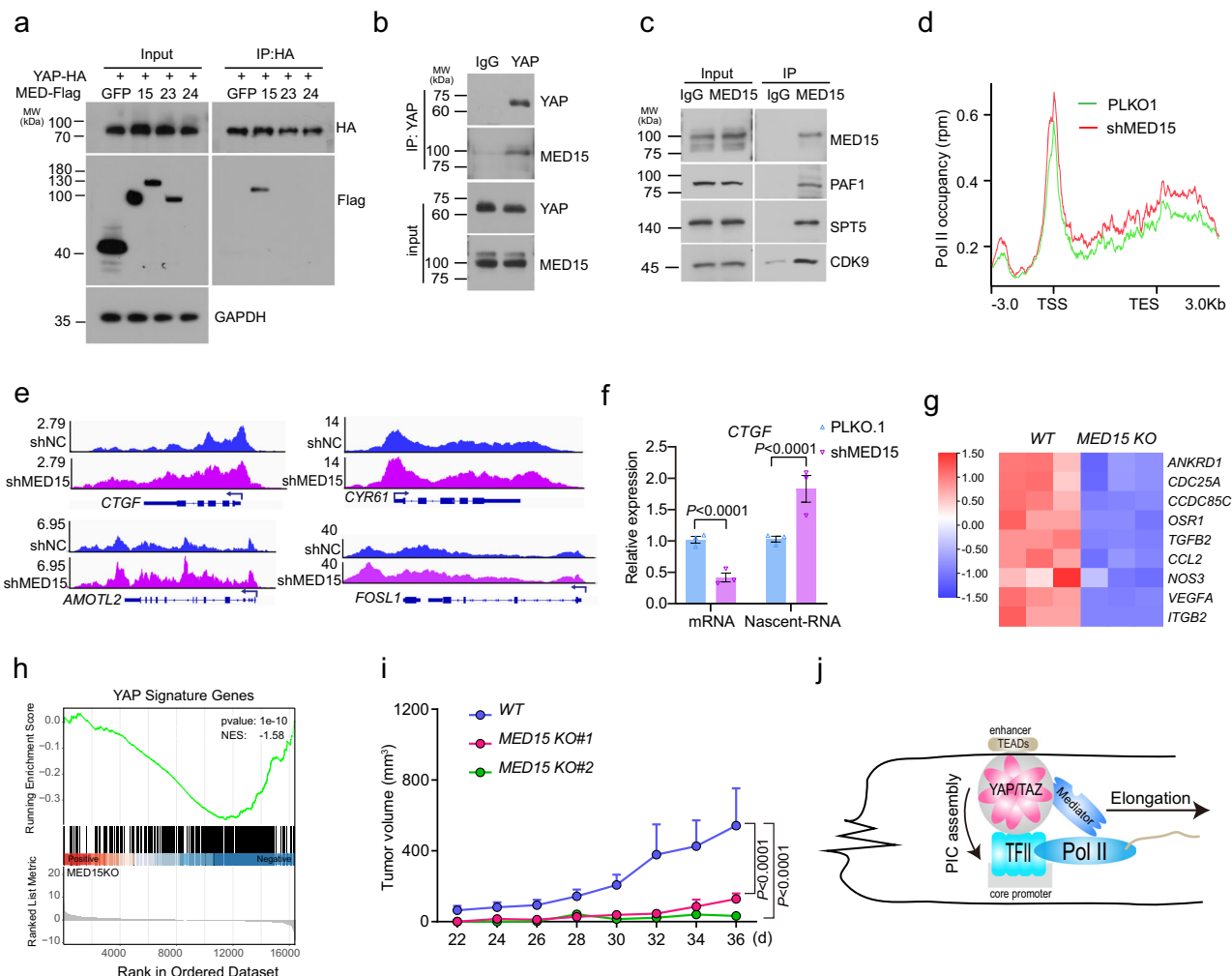
To determine whether the downregulation of target gene expression by TAF4 knockdown was associated with reduced Pol II loading on the transcription start site (TSS) regions of YAP/TAZ target genes, we performed cleavage under targets and tagmentation (CUT&Tag) analyses of Pol II occupancy in TAF4-or YAP/TAZ-knockdown cells. Indeed, as expected, TAF4 depletion led to a genome-wide reduction in Pol II enrichment at both the TSS and gene body, supporting the role of TAF4 as a broadly acting transcription initiation factor belonging to the TFIID family (Fig. 3k down, and Supplementary

Fig. 7e, f). In contrast, siYAP/TAZ had a smaller impact on Pol II, with the most significant changes observed in Pol II occupancy at YAP target genes, indicating that YAP primarily regulates its specific target genes by interaction with TAF4 (Fig. 3k up and Supplementary Fig. 7g–j). For instance, Pol II occupancy at the typical target loci—*CYR61*, *CTGF*, *MYC*, *AMOTL2*, and *CDI55*—was reduced in TAF4- or YAP/TAZ-knockdown cells (Fig. 3l and Supplementary Fig. 7k).

In summary, the TADs of YAP/TAZ initiate Pol II loading for target gene transcription through TAF4 dependent Pol II loading, where the TAD-TAF4 interaction is heavily reliant on hydrophobic interactions, specifically involving a hydrophobic pocket on TAF4 and the helix, and FLTWL on YAP-TAD.

### TADs of YAP/TAZ recruit MED15 for Pol II efficient elongations

In addition to TAF4, our interactome results showed potential interactions of mediator components, including MED1, MED15, and MED23, associated with the TAD of YAP (Fig. 3a). Previous studies have suggested a role for the mediator complex in facilitating Pol II release from promoters at YAP target loci<sup>31</sup>. This prompted us to explore whether the TAD of YAP directly recruits the mediator. Through an immune coprecipitation assay, we observed that YAP interacted with MED15, but not with MED23 or MED24 (Fig. 4a, b). Further examination of the interaction regions of MED15 and YAP revealed that the deletion of TAD completely abolished their interactions (Supplementary Fig. 8a). To explore the function of MED15 in YAP transcriptional activation, we performed a BioID assay to determine its spatial interactome (Supplementary Fig. 8b). As expected, we identified more than ten mediator components and numerous Pol II elongation factors (Supplementary Fig. 8c, d), suggesting that the mediator complex recruited elongation factors for YAP target gene elongation. Co-IP assays demonstrated that MED15 interacts with elongation factors such as PAF1, SPT5, and CDK9 (Fig. 4c). These interactions prompted us to examine the function of MED15 in Pol II elongation at the YAP target loci using the CUT&Tag assay. Knockdown of MED15 resulted in the downregulation of target genes (Supplementary Fig. 8e), and reduced Ki67 staining due to impaired growth (Supplementary Fig. 8f, g). Moreover, reconstitution of YAP/TAZ did not restore the YAP target gene reduction by MED15 depletion, suggesting that MED15 functions downstream of YAP/TAZ (Supplementary Fig. 8h). CUT&Tag analysis revealed that MED15 knockdown increased both the TSS and gene body occupancy of Pol II in several YAP/TAZ target genes, including *CTGF*, *CYR61*, *AMOTL2*, and *FOSL1* (Fig. 4d, e). However, increased Pol II loading at target loci led to decreased target gene expression, reminiscent of previous findings, wherein the loss of PAF1 and SPT5 resulted in inefficient Pol II elongation<sup>32</sup>. To explore whether MED15 depletion leads to inefficient elongation, we examined premature termination events in the classic target gene *CTGF* by comparing the levels of nascent RNA and mRNA using RT-qPCR. The results revealed an increased ratio of nascent RNA to mRNA, indicating the inefficient elongation of Pol II on the target gene bodies (Fig. 4f). The above results implicate an MED15-involving YAP transcriptional



**Fig. 4 | TADs of YAP/TAZ recruit MED15 for Pol II efficient elongations.** **a** HA-YAP was co-expressed with Flag-MED15/MED23/MED24 and subjected to coimmunoprecipitation assay ( $n = 3$  independent experiments). **b** Endogenous Co-IP of MED15 and YAP in NCI-H1299 cells ( $n = 3$  independent experiments). **c** Endogenous Co-IP of PAF1, SPT5, CDK9 and MED15 in NCI-H1299 cells ( $n = 3$  independent experiments). **d** Metagenome profile of Pol II CUT&Tag reads of YAP/TAZ target genes ( $n = 150$ ). **e** Representative genome browser tracks of Pol II CUT&Tag in NCI-H1299 PLKO.1 or shMED15 cells. **f** RT-qPCR was used to detect both mature mRNA and nascent RNA levels of *CTGF* in NCI-H1299 PLKO.1 or shMED15 cells ( $n = 3$  biological replicates). For nascent RNA detection, the reverse transcription primer was

designed to target the first intron of *CTGF*, 87 nucleotides downstream of the transcription start site (TSS). Expression levels were normalized to *GAPDH*. **g** Heatmap shows YAP target genes of NCI-H1299 MED15 KO or WT cells. **h** GSEA analysis of YAP signature genes from RNA-seq data of NCI-H1299 WT and MED15 knockout cells. **i** Tumor growth of NCI-H1299 WT or MED15 KO cells in xenograft models ( $n = 5$  mice). **j** Model depicting YAP/TAZ-TAD promotion of PIC assembly through TAF4 and Pol II elongation via MED15. Data are presented as mean  $\pm$  SEM. Statistical analysis was performed using 2-tailed Student's *t* test (**f**), and two-way ANOVA (**i**).

activation process, necessitating a deeper understanding of the underlying mechanisms.

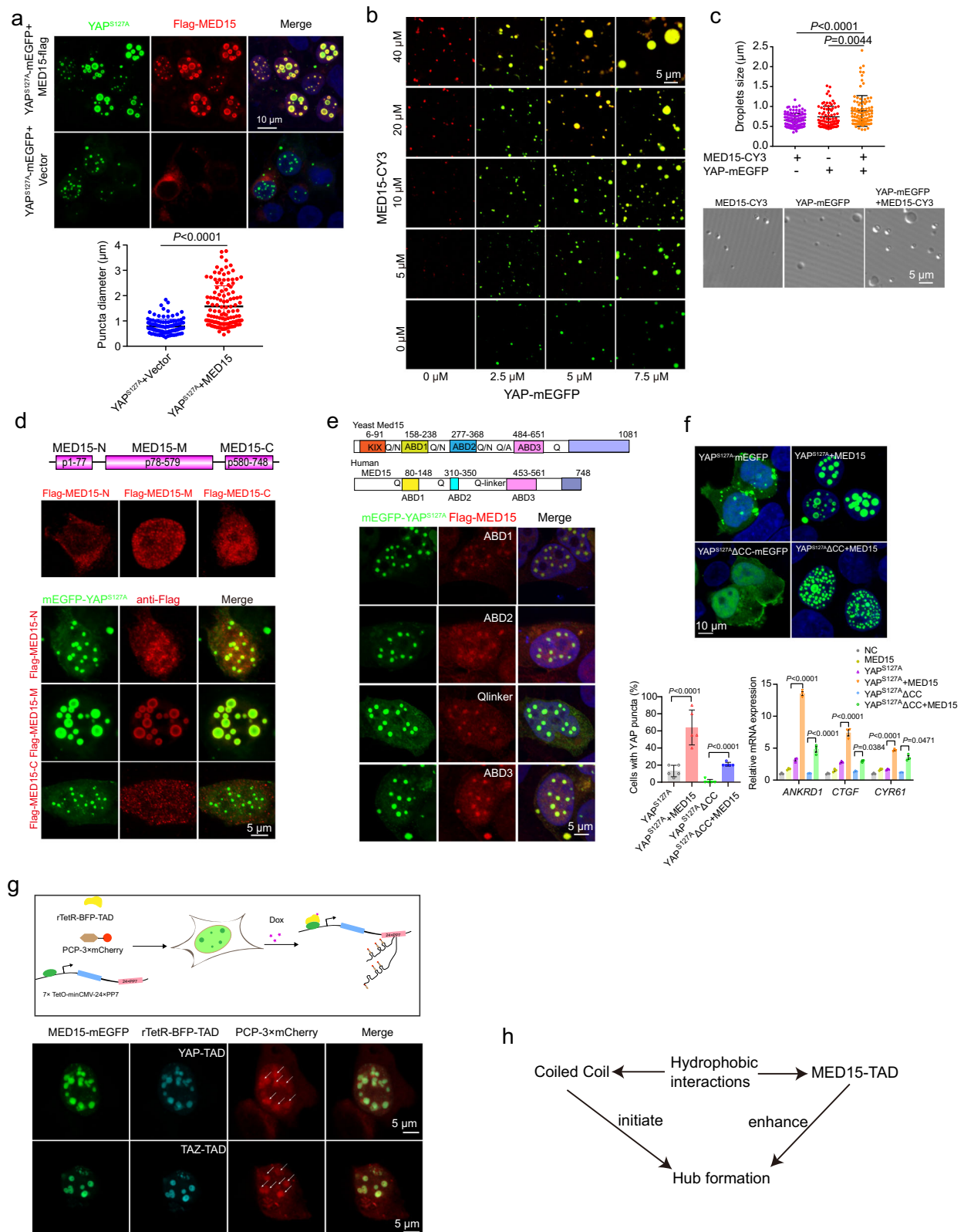
To evaluate the function of MED15 in YAP-associated transcription, tumor cell growth, and tumorigenesis in vivo, we established MED15 knockout cell lines in NCI-H1299 cells in a CRISPR-Cas9 dependent manner (Supplementary Fig. 8i). Initially, we compared the transcriptomes of *MED15* KO and WT cells. The profiles revealed significant downregulation of several YAP target genes associated with cancer initiation and the progression of immunosuppressive genes (Fig. 4g). Moreover, GSEA analysis revealed that MED15 depletion downregulated YAP signature genes (Fig. 4h). To evaluate the function of MED15 in cell growth in vivo, we performed xenograft assays and observed that the knockout of MED15 robustly reduced the growth rate of tumor cells (Fig. 4i and Supplementary Fig. 8j, k). Additionally, restoring MED15 expression in NCI-H1299 *MED15*<sup>-/-</sup> cells, rescued tumor growth defects (Supplementary Fig. 8l, m). Collectively, these findings indicate that MED15 is indispensable for the oncogenic

transcriptional program regulated by YAP and for tumor cell growth, likely due to its role in transcriptional elongation.

Taken together, TADs of YAP/TAZ have dual functions in initiation and elongation by recruiting TAF4 and Mediator 15 (Fig. 4j).

### The hydrophobic interaction of YAP-TAD and MED15 boosts transcriptional hub formation by co-condensations

Multiple reports support the notion that YAP/TAZ functions as a transcriptional hub through coiled-coil (CC) domain-mediated phase separation facilitated by hydrophobic interactions. Key transcription regulators are recruited to the condensates for efficient transcription in a spatially partitioned manner<sup>24,33–35</sup>. This prompted us to test whether MED15 was recruited to YAP condensates. Interestingly, in contrast to other mediator components, MED15 was recruited as well as boosting YAP condensation, including increased condensate size and number when co-expressed with YAP (Fig. 5a and Supplementary Fig. 9a, b). To examine whether co-condensation and enhancement occurred in vitro, we synthesized and purified YAP and MED15



(Supplementary Fig. 9c). Upon mixing them in a physiological concentration of NaCl, we observed similar co-condensation and enhancement of YAP droplet formation (Fig. 5b, c). We further identified the region involved in the co-condensation of YAP and MED15 by co-expressing different regions of MED15 and YAP, which revealed that the middle fragment of MED15 is required for co-condensation (Fig. 5d). Previous studies in yeast have identified several activation-

binding domains (ABDs) in the middle region of MED15<sup>36,37</sup>. Multiple sequence alignment revealed three relatively conserved ABDs (ABD1-3) in human MED15. Individual expression of ABDs with YAP demonstrated obvious co-condensation in the nucleus, with ABD3 showing particularly pronounced effects (Fig. 5e). These results suggested that the hydrophobic interactions of MED15-YAP acted as another driving forces for YAP condensation paralleled to CC mediated hydrophobic



**Fig. 5 | The hydrophobic interaction of YAP-TAD and MED15 boosts transcriptional hub formation by co-condensations.** **a** Confocal sections of YAP<sup>S127A</sup>-mEGFP expressed with or without Flag-MED15, and scatter plot showed the puncta diameter ( $n = 24$  cells per group). **b** Fluorescence images of in vitro His-YAP-mEGFP (green) and His-MED15-CY3 (red) were mixed with the indicated module concentration in 10% PEG solution. **c** Plot shows mean droplet size. DIC images of His-YAP-mEGFP and His-MED15-CY3 mixture (1:1 at 5  $\mu$ M, 10% PEG) shows numerous droplets at room temperature in a coverslip chamber. **d** mEGFP-YAP<sup>S127A</sup> was expressed with Flag-MED15-N, Flag-MED15-M, and Flag-MED15-C. **e** Schematic representation of ABDs of MED15. mEGFP-YAP<sup>S127A</sup> was expressed with MED15-ABD1, ABD2, Linker, and ABD3. **f** Images of Flag-MED15 co-expressed with mEGFP-YAP<sup>S127A</sup>

or mEGFP YAP<sup>S127A</sup>ΔCC, histogram shows the ratio of cells with puncta ( $n = 100$  cells per group). RT-qPCR analysis of YAP target genes in cells transfected with Flag-MED15 (1  $\mu$ g), mEGFP-YAP<sup>S127A</sup> (200 ng) or mEGFP-YAP<sup>S127A</sup>ΔCC (200 ng) ( $n = 3$  biological replicates). **g** Schematic of visualizing transcriptional activation in YAP/TAZ-TAD and MED15 condensates. Arrows indicate the nascent RNA signals (bound by PCP-3×mCherry) colocalizing with TAD/MED15 condensates (rTetR-BFP-YAP/TAZ-TAD and mEGFP-MED15) after addition of doxycycline (0.01 mg/ml). **h** Schematic of the hydrophobic interaction of YAP and MED15 forming a transcriptional hub to regulate the transcription initiation and elongation. Data are presented as mean  $\pm$  SEM. Statistical analysis was performed using 2-tailed Student's *t* test (**a**), one-way ANOVA (**c**, **f**). Scale bars: 10  $\mu$ m (**a**, **f**), 5  $\mu$ m (**b**, **c**, **d**, **e**, **g**).

interactions. To test this hypothesis, we examined whether the condensation defect of YAP<sup>S127A</sup>ΔCC could be restored by co-expression with MED15. Surprisingly, MED15 co-expression with YAP<sup>S127A</sup>ΔCC restored its phase separation, subsequently rescuing its transcriptional activity defects (Fig. 5f). To test whether co-condensation drives transcription in the droplets, we fused the TAD of YAP/TAZ with rTetR, co-expressed it with PP7 coat protein (PCP)-3×mCherry and TetO-PP7, and visualized and monitored the levels of nascent RNA by microscopy<sup>38</sup>. We observed increased transcription in the condensates after doxycycline treatment (Fig. 5g).

These results indicated that the hydrophobic interactions of TAD-ABD3 enhanced YAP condensation parallel to CC-mediated hydrophobic interactions (Fig. 5h).

### The mechanism of interaction between TADs and MED15

To further understand elongation, we investigated the molecular mechanisms underlying the interactions between TADs and MED15. By performing multiple sequence alignments, we identified three relatively conserved ABDs (ABD1-3) in human MED15 (Fig. 5e). This result prompted us to examine whether YAP-TAD binds to MED15-ABDs in humans similarly to the fuzzy interactions observed in yeast. We prepared protein samples from MED15 and its ABDs (Supplementary Fig. 10a–e) and performed hydrogen-deuterium exchange (HDX) detected by mass spectrometry (MS) (HDX-MS) assays to analyze the binding sites on YAP and MED15. Unlike the fuzzy interactions in yeast, the results indicated that the TAD domain of YAP and the ABD3 domain of MED15 were the primary binding sites responsible for the YAP-MED15 interaction (Fig. 6a; Supplementary Fig. 10f–h, Supplementary Fig. 11a, b; Supplementary Fig. 12a, b; Supplementary Fig. 13a). Follow-up NMR titration assays confirmed that ABD1 and ABD2 did not bind YAP-TAD (Supplementary Fig. 13b, c). Consistent with our expectations, surface plasmon resonance (SPR) characterization revealed a substantial interaction between YAP-TAD and MED15 (particularly its ABD3 domain), evidenced by comparable dissociation constants ( $K_d = 27.5 \pm 14.8$  nM for MED15 and YAP,  $K_d = 160.2 \pm 54.3$  nM for YAP-TAD and ABD3; Supplementary Fig. 14a–c). These in vitro biophysical assays aligned with findings from co-condensation experiments for individual ABDs, prompting us to focus on ABD3-TAD interactions in subsequent studies.

To acquire detailed properties of the TAD-MED15 interaction, we assigned most of the backbone and side-chain chemical shifts of a standalone truncation of the ABD3 domain of MED15 (residues 453–561 of MED15 isoform 2, named MED15-ABD3) using NMR spectroscopy. We next determined the solution structure of MED15-ABD3 under PDB accession number 8J9A, which consists of a long N-terminal loop and three  $\alpha$ -helices (designated as  $\alpha$ 1,  $\alpha$ 2, and  $\alpha$ 3) (Fig. 6b and Supplementary Fig. 15a, b). Subsequently, we conducted 2D HSQC spectrum-based NMR titration experiments, using the CSPs observed during the titration of MED15-ABD3 into <sup>15</sup>N-YAP-TAD to identify the binding sites on YAP-TAD for the YAP-ABD3 interaction (Fig. 6c and Supplementary Fig. 16a). Notably, certain hydrophobic residues in the helix and C-terminal FLTWL of YAP-TAD exhibited significant chemical shift

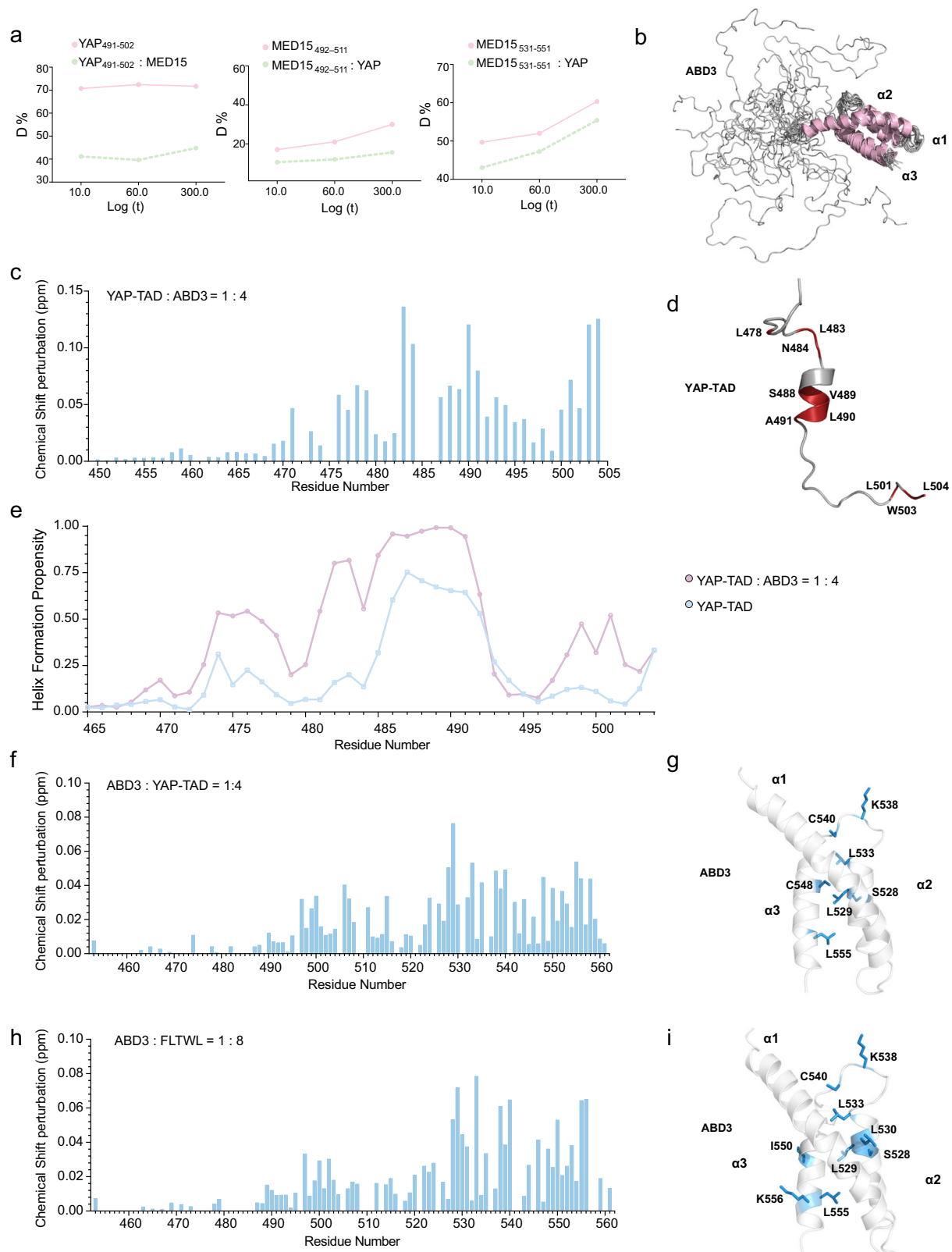
perturbations, indicating their involvement in the binding of MED15-ABD3 (Fig. 6c, d). Interestingly, ABD3 binding induced the elongation of the  $\alpha$ -helix of YAP-TAD (Fig. 6e). The extension of the secondary structural elements of the initially disordered region of YAP-TAD depicts the flexible and binding-ready nature of this dual-targeting transcriptional coactivator, reflecting its versatile use in various situations regarding the transcription processes.

Backbone assignments and the MED15-ABD3 structure enabled us to perform reverse NMR titrations where serial concentrations of YAP-TAD were titrated into <sup>15</sup>N-MED15-ABD3. These experiments revealed that residues involved in binding were scattered mainly on  $\alpha$ 2 and  $\alpha$ 3 helices, with the majority located at the helix-helix interfaces, forming a clustering pattern of a line-like continuum (Fig. 6f, g and Supplementary Fig. 16b). Similarly, titration involving <sup>15</sup>N-TAZ-TAD with MED15-ABD3, as well as its reverse titration, showed a similar binding pattern to interactions between YAP-TAD and MED15-ABD3 (Supplementary Fig. 16c–f). Based on these findings on the TAD-ABD3 interaction and TAD-TAF4 binding sites, we investigated the roles played by the helix and FLTWL motif of YAP-TAD in the TAD-ABD3 interaction by titrating peptides containing each specific fragment into <sup>15</sup>N-MED15-ABD3. The FLTWL peptide had a binding interface analogous to YAP-TAD on MED15-ABD3, with most binding residues being hydrophobic and positioned at the aforementioned helix-helix junction interface (Fig. 6h, i and Supplementary Fig. 17a). Contrary to the <sup>15</sup>N-YAP-TAD titration results (Fig. 6c, d), the  $\alpha$ -helix-based peptide showed reduced affinity for binding ABD3 in a standalone state, characterized by hardly observed CSPs or peak intensity changes (Supplementary Fig. 17b). This observation suggests a weaker  $\alpha$ -helix-ABD3 interaction compared to  $\alpha$ -helix-TAF4 binding (Supplementary Fig. 6c and Supplementary Fig. 17b), potentially reflecting differentiated binding mechanisms and preferences for the two target proteins. In summary, the coexistence of  $\alpha$ -helix and the FLTWL motif within the TAD promotes intermolecular interactions with its binding partners.

Collectively, among the three ABDs of MED15, ABD3 specifically bound to YAP-TAD, involving spatially neighboring residues on all three helices of ABD3 in the YAP-TAD with ABD3 interaction. Moreover, both the  $\alpha$ -helix and the FLTWL motif within YAP-TAD contribute to ABD3 binding, with the FLTWL motif interacting with MED15-ABD3 in a more independent way than the helix.

### Small peptides against TAD interaction inhibits tumor growth and sensitizes aPD-1 immunotherapy

Since the transcriptional activation of TADs of YAP/TAZ largely depends on hydrophobic interactions involving the FLTWL motif and  $\alpha$ -helix with cofactors, we aimed to selectively inhibit the transcriptional activity of YAP/TAZ using short peptides that compete for binding with these cofactors. To target nuclear interactions, we conjugated the nuclear localization sequence of SV40 (PKKKRKV) to small peptides using FITC for fluorescence imaging. Consequently, we synthesized four peptides based on stepwise-truncated  $\alpha$ -helix from YAP TAD (designated as TJ-H1 to TJ-H4), five peptides based on the FLTWL motif (TJ-C8, -C11, -C12, -M11, and -M12), and used SV40 alone as the



control peptide (TJ-SV40). For enhanced inhibitory efficacy, peptides TJ-M9 and TJ-M10 accommodated one copy each from the  $\alpha$ -helix and the FLTWL motif, whereas TJ-M11 and TJ-M12 included two copies from the FLTWL motif. Compared to the helix, FLTWL derivatives showed strong nuclear localization (Supplementary Fig. 18a–c) and interacted with MED15-ABD3 in a more independent manner than the helix (Supplementary Fig. 17a, b), which led us to select FLTWL derivatives

for further functional testing. After synthesizing these peptides, we encapsulated them in liposomes, which were characterized using cryo-electron microscopy (cryo-EM) and dynamic light scattering (DLS) (Fig. 7a and Supplementary Fig. 18d). Subsequently, NCI-H1299 cells were treated with various concentrations of liposome-packed peptides. Notably, both TJ-C8 and TJ-M11 exhibited biological activity against cell growth, with TJ-M11 exhibiting a lower IC<sub>50</sub> value, as

**Fig. 6 | The mechanism of interaction between TADs and MED15.** **a** HDX-MS characterization for identification of YAP-MED15 binding sites. Deuterium uptake plots of MED15 peptides (Region I: AA 492–511, +4 charge; Region II: AA 531–551, +5 charge) and YAP peptide (AA 491–502, +3) were measured in the presence and absence of their binding partners. Data are plotted as percent deuterium uptake versus time (logarithmic scale). Red and green plots represent the unbound and bound states, respectively ( $n = 3$  technical replicates). **b** NMR structure ensemble of MED15-ABD3 consisting of 20 lowest-energy models. **c** Analysis for the CSP of  $^{15}\text{N}$ -YAP-TAD upon titration with ABD3. **d** The residues with significant CSP during NMR

titration in (c) are mapped on the YAP-TAD structure in red. **e** Predicted helix formation propensity for YAP-TAD with or without ABD3 using TALOS-N webserver. **f** Analysis for the change in CSP of  $^{15}\text{N}$ -ABD3 upon titration with YAP-TAD. **g** The residues with significant CSP change during NMR titration in (f) are mapped on the MED15-ABD3 structure in blue. **h** Analysis for the change in CSP of  $^{15}\text{N}$ -ABD3 upon titration with the pentapeptide FLTWL. **i** The residues with significant CSP change in (h) during NMR titration experiment are mapped on the MED15-ABD3 structure in blue. Data are presented as mean  $\pm$  SD.

confirmed by the plate clone assay (Fig. 7b and Supplementary Fig. 18e). To dissect the structural mechanism of peptides competing for interactions with YAP, we performed NMR titration analysis using FLTWL on  $^{15}\text{N}$ -labeled TAFH and ABD3 of MED15. Indeed, FLTWL bound to the hydrophobic grooves of TAFH and ABD3 (Fig. 7c). In addition, we observed that TJ-M11 blocked the interactions of YAP with TAF4 and MED15 in cells through Co-immunoprecipitation (Fig. 7d, e). To evaluate whether TJ-M11 is associated with YAP transcriptional blockade, we performed RNA-seq analysis on NCI-H1299 cells treated with TJ-M11 (Supplementary Fig. 18f, g). RT-qPCR further confirmed that TJ-M11 disrupted the transcription of YAP target genes, including the immunosuppressive genes *CSF1*, *ITGB2*, and *IL33* (Fig. 7f and Supplementary Fig. 18h), highlighting its critical role in suppressing YAP-mediated transcription. These results indicate that TJ-M11 specifically blocks YAP transactivation by disrupting its TAD interactions with the cofactors MED15 and TAF4.

We further compared the activity of TJ-M11 in various cell lines, including de novo primary patient-derived lung adenocarcinoma cell lines and observed similar results (Fig. 7g). In contrast, TJ-M11 did not have a significant effect on NCI-H209 cells with low YAP expression<sup>39</sup>, suggesting minimal cytotoxicity (Supplementary Fig. 18i, j). Organoids derived from the cancer tissues of patients offer better clinical relevance for drug testing due to several advantages<sup>40</sup>. Therefore, we established organoids from independent surgical specimens and observed a strong nuclear localization of YAP with thyroid transcription factor 1 (TTF-1/NKX2-1), indicating YAP activation in these organoids (Supplementary Fig. 18k). To assess the antitumor activity of TJ-M11 in these organoid models, we treated the cells with different concentrations of TJ-M11 and examined their  $\text{IC}_{50}$  values. The results demonstrated that TJ-M11 effectively inhibited growth, albeit with a slightly higher  $\text{IC}_{50}$  value than in the 2D culture (Fig. 7h). Given the promising efficacy of TJ-M11 in several classical cell lines, patient-derived primary cell lines, and organoids in vitro, we evaluated its therapeutic efficacy in vivo using the rodent lung adenocarcinoma allograft model by grafting TDCL cells (Supplementary Fig. 2a) into immune-competent C57BL/6J mice, considering the key role of YAP in tumor cell proliferation and immunosuppression. As expected, TJ-M11 treatment significantly suppressed the tumor size. Our previous study showed the treatment of anti-PD-1 inhibitor to TDCL allograft tumors led to adaptive resistance due to YAP activations<sup>41</sup>. This promoted us to examine the efficacy of combination therapy of TJ-M11 with anti-PD-1 inhibitor. Indeed, the combination therapy showed stronger tumor inhibition effect than either monotherapy, indicating TJ-M11 reverses adaptive resistance of anti-PD-1 inhibitor (Fig. 7i).

In summary, the small peptide mimicked the hydrophobic motif of FLTWL and inhibited tumor growth and enhanced immune attack of immunotherapy, indicating that dual targeting of the interactions of TADs of YAP/TAZ with cofactors is efficient for cancer therapy.

## Discussion

YAP/TAZ transcriptional control are regulated by multiple factors, including enhancer binding, SWI/SNF chromatin remodeling, and

phosphorylation<sup>42–44</sup>. YAP/TAZ recruit BRD4 and RNA polymerase II to regulate transcription at both promoters and enhancers<sup>45</sup>, with CDK7 phosphorylation enhancing their activity at enhancer regions<sup>46</sup>, thereby promoting tumor progression. In this study, we characterized the core TAD of YAP (450–504), which is shorter than the previously reported YAP TAD (291–504)<sup>47</sup>, further elucidating its role in tumorigenesis. We found that TADs serve dual functions in transcription activation: they facilitate transcription initiation through TAF4-dependent Pol II loading and enhance elongation via MED15-dependent Pol II elongation at target loci. These findings provide additional insights into the mechanisms underlying YAP transcriptional activation.

Previous studies have shown that YAP/TAZ recruit Pol II through the Mediator complex (MED1), promoting CDK9-mediated phosphorylation of Pol II to regulate transcription elongation<sup>31</sup>. However, the precise mechanism of this interaction remains unclear. Structurally, we reveal that YAP mediates its interaction with MED15 through its TAD domain. These interactions are primarily driven by hydrophobic forces involving the  $\alpha$ -helix and the FLTWL linear motif. Unlike the yeast homolog of MED15, which interacts via multiple weak, fuzzy binding domains, human MED15 binds to ABD3 through stronger hydrophobic interactions, a difference likely linked to TAD variation. Although FLTWL has been identified as a PDZ binding motif critical for YAP nuclear localization, our endogenous TAD knockout experiments showed no significant changes in YAP's subcellular distribution or protein stability (Supplementary Fig. 2b–d). Instead, the loss of TADs led to downregulation of YAP target genes, impaired tumor growth, and an enhanced immune response, suggesting that both the  $\alpha$ -helix and FLTWL motif are crucial for transcriptional activation. Additionally, our BioID interactome and Co-IP experiments further support the idea that YAP-TAD recruits elongation factors through the Mediator complex (MED15), which regulates Pol II elongation by recruiting the PAF1 and SPT5 complexes. Future studies should focus on elucidating the mechanisms by which the Mediator complex recruits these elongation factors.

Transcriptional hub formation with a high local concentration of transcriptional activators and Pol II is essential for high expression levels of target genes involved in numerous biological processes, such as development, stem cell renewal, and stress response. The IDRs of TAD mediated interactions are broadly accepted as the driving force of hub formation<sup>12,48</sup>. However, the mechanism through which IDRs induce the hub formation remains unclear. Recently, IDR mediated biomolecular condensation has been extensively studied for hub formation and transcriptional regulations<sup>49,50</sup>. In contrast, John Ferrie et al. hypothesized that IDR mediated self-enrichment binding is crucial for local high concentration, but that condensations by higher concentrations of transcription coactivators disrupts cellular genes transcription<sup>48,51,52</sup>. The results described here and in previous studies<sup>24</sup> support the model that the hydrophobic interactions of the CC domain mediates YAP condensations and the TADs mediated hydrophobic interaction with MED15 enhances YAP condensations. Unfortunately, MED15 antibodies are only lightly specific for immunofluorescence, genomic tag MED15 cell line establishment were unsuccessful in our hands, which limited us detect endogenous condensates. As an alternative, we expressed low levels of YAP and MED15

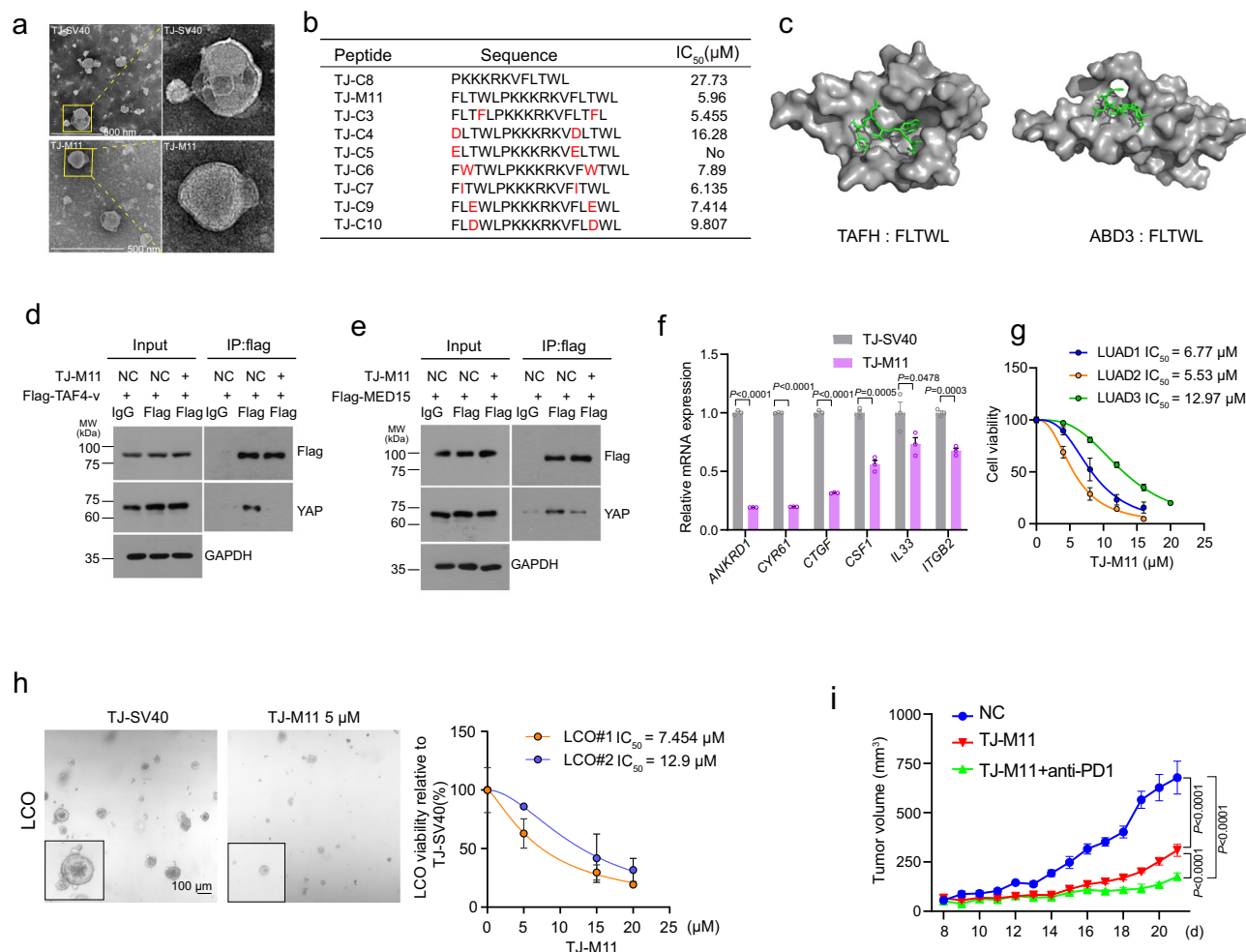


**Fig. 7 | Small peptides against TAD interaction blocked transactivation activity and suppressed tumor growth.** **a** Cyro-EM image of TJ-SV40 and TJ-M11. **b** IC<sub>50</sub> values of liposome-delivered peptides were measured with CCK8 in NCI-H1299 cells (48 h). **c** Molecular docking model of AlphaFold2-predicted TAFH structure with FLTWL peptide (left), and molecular docking model of MED15-ABD3<sub>484-561</sub> NMR structure with FLTWL peptide (right). HEK293T cells treated with TJ-SV40 or TJ-M11 in serum-free media for 12 h, then transfected with Flag-TAF4-v (d) or Flag-MED15 (e) for 48 h, subsequently, subjected to coimmunoprecipitation assays (*n* = 3 independent experiments). **f** RT-qPCR analysis of indicate genes expression in NCI-H1299 cells treated with 4 μM TJ-M11 or TJ-SV40 for 48 h (*n* = 3 biological replicates). **g** Viability of primary patient-derived lung adenocarcinoma (LUAD) cells treated with TJ-M11 or control for 48 h (*n* = 3 biological replicates). **h** Brightfield images of organoids plated in 96-well plates for TJ-M11 treatment. Organoids were treated with TJ-M11 or TJ-SV40 for 8 days, and relative LCO viability was assessed using CellTiter-Glo (*n* = 3 biological replicates). **i** The effect of TJ-M11 supplementation on PD-1 blockade therapy in TDCL tumor-bearing C57BL/6 mice (*n* = 5 or 6 mice per group). Data are presented as mean ± SEM. Statistical analysis was performed using 2-tailed Student's *t* test (f) and two-way ANOVA (i). Scale bars: 500 nm (a); 100 μm (h).

to mimic endogenous protein levels. Thus, our findings clarify that TADs of YAP/TAZ as the key effector domains for transcriptional output, converge on the hydrophobic interactions with cofactors not only for transcriptional initiation and elongation, but also for hub formation. In the future, we will dissect the dynamics and function of YAP-MED15 condensates in endogenous and physiological conditions.

Although several potent TFs have been shown to play critical roles in disease pathogenesis, targeting them for therapeutic applications remains a pressing challenge<sup>23</sup>. Unlike enzymes and membrane proteins, which are frequently targeted by drugs, TFs display properties that are unfavorable for drug targeting. However, because the Hippo signaling pathway plays an important role in tumorigenesis and cancer progression, inhibition of the complex of YAP and TEAD family TFs has been proposed as a promising therapeutic approach for a broad range of cancers<sup>5,20</sup>. However, developing drugs targeting these areas of the TEAD for cancer treatment can be challenging because of the shallow pockets on the surface and the central pocket with a covalently bound lipid ligand<sup>23</sup>. To address this challenge, it is essential to improve drug target discovery and optimize therapeutics. In the present study, we

successfully validated two PPIs, YAP-TAF4 and YAP-MED15, as targets for cancer drug development. Notably, we observed that YAP-TAD, especially the FLTWL motif, acts as a dual-target binding component against TAF4 and MED15. Considering this, we designed FLTWL-mimicking peptides incorporating SV40, which are capable of targeting both TAF4 and MED15 in the nucleus. These peptides, including the most potent peptide, TJ-M11, inhibited the interaction between YAP and both TAF4 and MED15, leading to decreased tumor cell growth in vitro and in vivo. Targeting TJ-M11 showed a clear dependence on YAP activity, as the peptide had no significant effect on the viability of HeLa and NCI-H209 cells. In addition to developing small peptide inhibitors, we discovered several potential hydrophobic regions on the YAP-binding interface of MED15 and TAF4 that could serve as targets for future inhibitor development. Our peptide inhibitor, TJ-M11, did bind to TAF4 and MED15, inhibit both transcription initiation and elongation, and suppress tumor growth in a mouse model. These results validate our dual-targeting inhibitor as a potential option for resistance-suppressing cancer therapy. Systematic screening using the luciferase system and a computer-aided drug design system in the



future would be useful for developing more efficient and clinically applicable YAP/TAZ-based inhibitors.

Methods

Cell lines

Human lung adenocarcinoma cell lines (NCI-H1299, A549, NCI-H1975), the human small cell lung cancer cell line NCI-H209, the mouse Lewis lung cancer (LLC), the human cervical cancer cell line HeLa, and the human embryonic kidney cell line 293 T (HEK293T) were purchased from Pricella (Wuhan, China). The TDCL cell line was previously constructed by our research group<sup>26</sup>. HEK293T and HeLa cells were cultured in high glucose (4.5 g/l) Dulbecco's modified Eagle's medium (DMEM; Gibco). NCI-H1299, A549, NCI-H1975, NCI-H209, LLC and TDCL cells were maintained in RPMI 1640 Medium. All cells were cultured in media supplemented with 10% Fetal Bovine Serum (FBS; HyClone), 100 U/ml penicillin and 100 µg/ml streptomycin (Gibco) and incubated at 37 °C in a humidified atmosphere with 5% CO<sub>2</sub>.

Mice

All animals were housed under specific pathogen-free conditions in automated watered and ventilated cages on a 12 h light/dark cycle, and handled in accordance with the guidelines of the Institutional Animal Care and Use Committee of the Huazhong University of Science and Technology. The mice used in this study were purchased from Gem-Pharmatech Co., Ltd. (Nanjing, China), including 6-week-old BALB/c nude mice (male), 6-week-old C57BL/6J mice (male), and 7-week-old immunodeficient NOD/ShiLtJGpt-Prkdc<sup>em26Cd52</sup>Il2rg<sup>em26Cd22</sup>/Gpt (NCG) mice (male). Tumors were allowed to establish, sizes (average ~50 mm<sup>3</sup>) were matched, and then the mice were randomly allocated to groups of 6–10 animals. Based on our previous experience, around 6–10 animals were used in each group, as this quantity allowed us to obtain statistically significant data while keeping the number of animals used to a minimum. Tumor size was determined by taking caliper measurements of tumor length, width and tumor volume was calculated as volume = 0.5 × length × width<sup>2</sup> (mm<sup>3</sup>). Tumor size did not exceed 1500 mm<sup>3</sup>.

Lung Adenocarcinoma (LUAD) patient specimen

The patients included in the study provided written informed consent for the use of the specimen. The studies were performed in accordance with the Medical Ethics Committee of Tongji Medical College, Huazhong University of Science and Technology. Patient-derived tumor cells and organoids used for TJ-M11 treatment are shown below (Table 1):

Tumor model

Healthy male C57BL/6J mice or BALB/c nude mice at the age of 6–7 weeks were maintained in pathogen-free conditions, and allowed to acclimate for 1 week before being used. During the tumor formation assay, TDCL *WT* and *Yap-ΔTAD Taz*<sup>-/-</sup> cells (1.5 × 10<sup>6</sup>) were injected into the flank of the C57BL/6J or NCG mice subcutaneously. NCI-H1299 *WT* or *MED15*<sup>-/-</sup> cells (6 × 10<sup>6</sup>) were injected into the flank of the BALB/c nude mice subcutaneously. Once tumors were detected (average ~50 mm<sup>3</sup>), tumor volume was measured by vernier calipers. For CD8<sup>+</sup>

T-cell depletion experiment, 100 µg of anti-mouse CD8α antibody (BioXCell, BE0061) was intraperitoneally injected 2 days before tumor inoculation and continued every three days until the tumor size reached the end point.

For peptide supplementation with PD-1 blockade therapy, TDCL cells (1 × 10<sup>6</sup>) were injected subcutaneously into the flank of the C57BL/6J mice. Once tumors were detected (average ~50 mm<sup>3</sup>), the mice were intratumorally injected every other day with liposome-derived TJ-SV40 or TJ-M11 (5 mg/kg) peptides followed with 200 µg anti-PD-1 antibody (Selleck, A2122) every three days. Tumor diameters were measured using calipers and the volume was calculated by 0.5 × length × width<sup>2</sup>. Mice were sacrificed after three weeks, and tumor weights were then measured.

UAS-Luc transcription assay

HEK293T cells were seeded into 96-well plates, transfected with Gal4-YAPTAD (100 ng) and 40×UAS-Luc (100 ng) and PLR-TK (2 ng) plasmids using polyethylenimine (PEI) for 36 h and harvested for the measurement of luciferase activity. The internal transfection control *Renilla* was used to normalize the luciferase activities to control for differences in transfection efficiency.

Western blot and co-immunoprecipitation

These western blot experiments were performed as previously described. Briefly, cells were harvested and lysed with 1% SDS on ice and subsequently heated at 98 °C for 20 min. Centrifuged at 12,000 *g* for 15 min and collected the supernatant. Samples were subject to SDS-PAGE. Immunoblot analysis was performed with specific antibodies and secondary anti-mouse or anti-rabbit anti-bodies conjugated to horseradish peroxidase (HRP). Visualization was achieved with chemiluminescence.

For Co-IP, HEK293T cells were grown in 10 cm dishes and transfected with the appropriate plasmids for 48 h. Collected cells and lysed with 1 ml Western-IP lysis buffer (Beyotime, P0013) containing protease inhibitor cocktail and PMSF. The lysates were subsequently sonicated on ice for 60 s. The lysates were centrifuged at 12,000 *g* at 4 °C for 10 min. 100 µl of the lysates were saved as input to detect the expression of target proteins. 900 µl of the supernatants were incubated with 1 µl of antibody and 20 µl protein G agarose beads (Millipore, 16-226) on a rotator overnight at 4 °C. The lysates were washed by lysis buffer for six times, then the immunoprecipitated complexes were resuspended in 50 µl 3 × reducing sample buffer and boiled at 95 °C for 5 min. After centrifugation to pellet the agarose beads, supernatants were subjected to SDS-polyacrylamide gel electrophoresis (PAGE). All experiments are independently repeated at least 3 times.

The antibodies used for immunoprecipitation (IP) and immunoblotting (IB) are as follows: mouse monoclonal antibody to Flag (M2) (Sigma-Aldrich, F3165, 1:1000 for IP), rabbit monoclonal anti-HA tag (C29F4) (Cell Signaling, 3724 1:1000 for IP), rabbit monoclonal antibody to YAP1 (Cell Signaling, 14074, 1:2000 for WB), rabbit antibody to TAZ (V386) (Cell Signaling, 4833, 1:1000 for WB), rabbit antibody to TAZ (Cell Signaling, 83669, 1:2000 for WB), MED15 (Proteintech, 11566-1-AP), TAF4 (Biodragon, BD-PT4527), SPT5 (Abclonal, A19225, 1:1000 for WB), PAF1 (Abclonal, A3437, 1:1000 for WB), CDK9 (Abclonal, A11145, 1:1000 for WB).

BioID analysis

BioID assay was performed as standard protocols<sup>53,54</sup>. HEK293T cells were plated in 10 cm dishes and transfected with BirA\*-Gal4-YAP-TAD and UAS-luciferase plasmids for 12 h, then incubated in complete media supplemented with 50 µM biotin for another 24 h. Removed the media and washed the cells with cold PBS for six times, collected the cells and lysed in 1 ml lysis buffer containing protease inhibitor cocktail and PMSF. Subsequently sonicated on ice. The lysates were

**Table 1 | Patient characteristics for LUAD patient-derived tumor cells and organoids**

	Patient 1	Patient 2	Patient 3
Cancer type	LUAD	LUAD	LUAD
Age (years)	≥65	≥65	≤50
Gender	Female	Male	Male
TNM stage	T2aNOMO	T2aN2bMORO	T2bNOMORO
Tumor stage	IB	IIIA	IIA

centrifuged at 12,000 *g* for 10 min at 4 °C. A portion of supernatants (50  $\mu$ l) were saved as input. The rest of the lysates were incubated with 50  $\mu$ l streptavidin agarose beads (Thermo, TE264933) at 4 °C overnight. Beads were collected and washed twice at 25 °C with 1 ml 2% SDS.

Then rewashed twice with buffer I (0.1% deoxycholate, 1% Triton X-100, 500 mM NaCl, 1 mM EDTA, and 50 mM HEPES, pH 7.5), once with wash buffer II (250 mM LiCl, 0.5% NP-40, 0.5% deoxycholate, 1 mM EDTA, and 10 mM Tris, pH 8.1). This was followed by washing twice with wash buffer III (50 mM Tris, pH 7.4, and 50 mM NaCl). Then, 90% of the sample to be analyzed by mass spectrometry was washed twice in 50 mM  $\text{NH}_4\text{HCO}_3$ . The rest 10% of the sample was reserved for Western blot analysis. Bound proteins were removed from the agarose beads with 50  $\mu$ l sample buffer saturated with biotin at 98 °C.

### Flow cytometry

Fresh TDCL tumor tissues were dissected and cut into pieces by scissors, then digested in PBS which containing 0.2 mg/ml collagenase IV (Invitrogen, 17104019) and 0.04 mg/ml DNase I (Roche, 10104159001), incubate in shaker at 37 °C and 200 rpm for 1 h. Pipet and filtrate the tumor tissues to achieve single cell suspension. Centrifuge at 400 *g* for 5 min, remove the supernatant and lyse the blood cell with ACK buffer (GIBCO, A1049201). Lymphocytes were enriched by centrifugation of the cell suspension with 40% percoll gradient (GE healthcare, No.17-0891-01) in DMEM at 550 *g* for 35 min. Resuspend the cells in 600  $\mu$ l culture medium supplemented with PMA (20 ng/ml), Ionomycin (1  $\mu$ g/ml), golgi inhibitor (1: 1000) at 37 °C incubator. Collected cells were firstly stained with Fixable Viability Dye-eFluor 506 (eBioscience, 65-0866-14). After washing with PBS, cells were stained with surface antibodies including CD45-percp/Cy5.5 (BioLegend, Clone 30-F11), anti-CD3-APC (BioLegend, Clone 17A2), anti-CD8a-PE/Cy7 (BioLegend, Clone 53–6.7) for 20 min at room temperature. Then cells were washed and permeabilized in 150  $\mu$ l Fixation/perme solution (Biolegend, 420801) at 4 °C for 40 min, washed with the Perm/Wash buffer (Biolegend, 421002), and then stained with anti-IFN $\gamma$ -Bv421 (BioLegend, Clone XMGL2), anti-GZMB-FITC (BioLegend, Clone GB11) for 1 h. Cells were washed and resuspended in Perm/Wash buffer and were read on a flow cytometer (BD FACSVerse). Data were analyzed using FlowJo software (Version 10).

### In vivo OVA-specific CD8<sup>+</sup> T cells analysis

Ovalbumin expressing (OVA<sup>+</sup>) tumor cells were established by infection tumor cells with the lentivirus expressing ovalbumin and nanoluciferase (Luc). Infected cells were selected with blasticidin (InvivoGene, ant-bl-05) and their intracellular luciferase activities were quantified using RT-qPCR to ensure the comparable OVA expression across different groups of cells.

Equal numbers of OVA-expressing TDCL *WT* and *Yap*  $\Delta$ *TAD Taz*<sup>-/-</sup> cells were injected subcutaneously (s.c.) into the flank of the C57BL/6j mice. After 21 days, T cells were harvested from the tumor and stained with Flex-T biotin H-2Kb/OVA (257-264) tetramer (BioLegend, 280051) and anti-CD8 antibody for tumor-specific T cells by flow cytometry.

### Lung cancer organoids (LCOs) establishment and drug treatment

LCOs were cultured according to standard protocols<sup>55</sup>. Briefly, LCOs were cultured in 24-well plates over 2 weeks were harvested and dissociated using TrypLE Express. The dissociated LCOs were mixed in organoid medium+ Matrigel (1:1 ratio) and seeded onto 96-well white plates (10  $\mu$ l of  $2 \times 10^3$  cells per a well; Corning). After gelation, 100  $\mu$ l organoid medium was added to each well. The LCOs were allowed to grow for 7–10 days. Then, liposomes delivered TJ-M11 and TJ-SV40 control were added every three days in triplicate. After 6 days, the medium was changed to 100  $\mu$ l organoid medium per well to measure cell viability, and 100  $\mu$ l CellTiter-Glo (G9681, Promega) was added to

each well. The plates were agitated for 30 min at room temperature prior to luminescence reading. The determination of IC<sub>50</sub> values was conducted using GraphPad Prism.

### NMR data collection, structure determination, relaxation and titration experiments

All NMR experiments in this study were conducted on an Avance III 600 MHz spectrometer (Bruker) equipped with a <sup>1</sup>H/<sup>13</sup>C/<sup>15</sup>N-TCI cryogenic probe (Bruker) at 25 °C. <sup>13</sup>C/<sup>15</sup>N-labeled protein was exchanged to NMR buffer A (20 mM HEPES, 100 mM NaCl, 2 mM TCEP, 0.1 mM DSS, 5% D<sub>2</sub>O, pH 7.0) and concentrated to 0.43 mM to collect NMR spectra for backbone and side chain assignments. For <sup>15</sup>N-edited NOESY-HSQC, a <sup>15</sup>N-labeled 1.0 mM protein sample in NMR buffer A was used instead. For NMR titration, both <sup>15</sup>N-labeled human YAP transactivation domain and unlabeled MED15 were prepared in NMR buffer B (20 mM HEPES, 150 mM NaCl, 2 mM TCEP, 6% D<sub>2</sub>O, pH 7.5).

Collectively, 2D <sup>1</sup>H-<sup>15</sup>N-HSQC and 3D HNCACB, CBCA(CO)NH, HNCA, and HNCO spectra were recorded for backbone assignment, while 2D <sup>1</sup>H-<sup>13</sup>C-HSQC and 3D HBHA(CO)NH, (H)CCH-TOCSY spectra were acquired for side-chain assignment. A <sup>15</sup>N-edited NOESY-HSQC experiment with a mixing time of 130 ms was conducted to obtain NOE cross-peaks, in which signal heights were imported to Aria2<sup>56</sup> software to calculate NOE distance constraints. Spectra FIDs were processed by NMRPipe<sup>57</sup> software, and the following spectra were analyzed with POKY<sup>58</sup> software. Backbone torsion angle constraints were generated by TALOS-N<sup>59,60</sup> webserver using chemical shifts.

Structure calculation was performed using Aria2 with modified MD parameters: 20,000, 10,000, 50,000, and 40,000 steps for high-temp, refinement, cool1 and cool2 sessions, respectively. The final iteration samples 250 structures, from which 20 models of lowest energy were calculated to be the final ensemble. The following structural evaluation was conducted by PROCHECK software<sup>60</sup>. PyMol software (The PyMOL Molecular Graphics System, Version 2.5.5 Schrödinger, LLC.) was applied for structure visualization.

All NMR titration experiments were conducted by using a <sup>15</sup>N-protein sample as the analyte and adding protein ligand samples in natural abundance into the <sup>15</sup>N-protein sample to reach serial molar ratios of these two proteins, and the <sup>1</sup>H-<sup>15</sup>N-HSQC spectrum before titration and at each titration point was recorded. In the titration experiment involving <sup>15</sup>N-YAP-TAD with MED15-ABD1/2/3, respectively, 100  $\mu$ M <sup>15</sup>N-YAP-TAD was titrated with 0, 0.5, 1, 2, and 4 equivalent MED15-ABD1/2/3 in a molar ratio, respectively. In the titration experiment involving <sup>15</sup>N-YAP-TAD with MED15, 80  $\mu$ M <sup>15</sup>N-YAP-TAD was titrated with 0, 1 equivalent MED15 in a molar ratio. In the titration experiment involving <sup>15</sup>N-YAP-TAD with M1, TAF4<sub>582-837</sub>, and TAFH, respectively, 100  $\mu$ M <sup>15</sup>N-YAP-TAD was titrated with 0, 0.5, 1, 2, and 4 equivalent M1, TAF4<sub>582-837</sub>, and TAFH in a molar ratio, respectively. In the titration experiment involving <sup>15</sup>N-TAZ-TAD with MED15-ABD2/3, respectively, 100  $\mu$ M <sup>15</sup>N-TAZ-TAD was titrated with 0, 0.5, 1, 2, and 4 equivalent MED15-ABD2/3 in a molar ratio, respectively. In the titration experiment involving <sup>15</sup>N-TAZ-TAD with MED15, 80  $\mu$ M <sup>15</sup>N-TAZ-TAD was titrated with 0, 1 equivalent MED15 in a molar ratio. In the titration experiment involving <sup>15</sup>N-TAFH with YAP-TAD, 100  $\mu$ M <sup>15</sup>N-TAFH was titrated with 0, 0.5, 1, 2, and 4 equivalent YAP-TAD in a molar ratio. In the titration experiment involving <sup>15</sup>N-TAFH with chemically synthesized peptide sequences for SDILNDMESVLAATK without any modifications, 100  $\mu$ M <sup>15</sup>N-TAFH was titrated with 0, 1, 2, 4, and 8 equivalent SDILNDMESVLAATK in a molar ratio. In the titration experiment involving <sup>15</sup>N-TAFH with chemically synthesized peptide sequences for FLTWL without any modifications, 100  $\mu$ M <sup>15</sup>N-TAFH was titrated with 0, 1, 2, 4, and 8 equivalent FLTWL in a molar ratio. In the titration experiment involving <sup>15</sup>N-MED15-ABD3 with YAP-TAD, TAZ-TAD, respectively, 100  $\mu$ M <sup>15</sup>N-MED15-ABD3 was titrated with 0, 0.5, 1, 2, and 4 equivalent YAP-TAD, TAZ-TAD in a molar ratio, respectively. In the titration experiment involving <sup>15</sup>N-MED15-ABD3 with chemically

synthesized peptide sequences for SDILNDMESVLAATK without any modifications, 100  $\mu\text{M}$   $^{15}\text{N}$ -MED15-ABD3 was titrated with 0, 1, 2, 4, and 8 equivalent SDILNDMESVLAATK in a molar ratio. In the titration experiment involving  $^{15}\text{N}$ -MED15-ABD3 with chemically synthesized peptide sequences for FLTWL without any modifications, 100  $\mu\text{M}$   $^{15}\text{N}$ -MED15-ABD3 was titrated with 0, 1, 2, 4, and 8 equivalent FLTWL in a molar ratio. For binding site identification, we analyzed the heights and chemical shifts of each residue peak in the  $^1\text{H}$ - $^{15}\text{N}$ -HSQC spectra recorded during titrations, and determined CSPs and ratio of peak intensities by comparing the spectra of apo- and holo-form analyte protein. The CSP was calculated using the following formula (1):

$$\Delta\delta = \sqrt{\frac{1}{2} \left[ (\Delta\delta_H)^2 + \left( \frac{\gamma_N}{\gamma_H} \Delta\delta_N \right)^2 \right]} \quad (1)$$

Where  $\Delta\delta_H$  and  $\Delta\delta_N$  represented chemical shift displacements for  $^1\text{H}$  and  $^{15}\text{N}$  nuclei observed upon titrations, respectively, and  $\gamma_N$  and  $\gamma_H$  represent gyromagnetic ratios for  $^1\text{H}$  and  $^{15}\text{N}$  nuclei, respectively. The change in peak intensity was quantified based on the ratio of the peak height of each residue before and after titration.

### Peptide docking calculation

A linear conformation of the FLTWL pentapeptide was generated using Avogadro and docked to AlphaFold2-derived TAF4 and MED15-ABD3 proteins using the HADDOCK 2.4 docking webserver (<https://doi.org/10.3389/fmolb.2021.729513>). All five residues of the FLTWL pentapeptide were designated as fully-flexible segments. The hydrophobic binding groove residues, including F599, L603, V620, L641, L645, L653, and F656, were designated as the active residues for docking with TAF4, as they were involved in the interaction. The NMR-derived binding interface residues (designated as “I503, L530, and L533”) were used as the active residues for docking with MED15-ABD3. The sampling parameters were set as follows: 10,000 structures for rigid body docking, 1000 structures for semi-flexible refinement, 500 structures for final refinement, and 200 structures for analysis. Other docking parameters were kept at their default settings. We manually validated and subsequently analyzed the first structure of each lowest-energy cluster.

### Surface Plasmon Resonance (SPR) experiment

SPR studies were performed using the Biacore T200 system (Cytiva) at 25 °C with a flow rate of 30  $\mu\text{L}/\text{min}$ . MED15 or MED15-ABD3 protein were immobilized onto the series S CM5 sensor chips (Cytiva) by amine-coupling chemistry to achieve an immobilization level of 6000–7000 or 800–1100 resonance units (RU), respectively. Ligands were flowed over the chip surface in the pH 7.2–7.4 buffer PBST (150 mM NaCl, 2.68 mM KCl, 8.1 mM  $\text{Na}_2\text{HPO}_4$ , 1.76 mM  $\text{KH}_2\text{PO}_4$ , 0.05% Tween), prepared at the indicated concentrations by dilution into running buffer with 60 s contact time, 300 s dissociation time. Regeneration was performed by injections of Glycine (pH 3.0) for 30 s at 30  $\mu\text{L}/\text{min}$  flow rate. Data were analyzed with the Biacore Insight Evaluation Software Version 3.0.12 using steady state affinity 1:1 binding model.

### RNA interference experiments

Lentivirus expressing short-hairpin RNAs was prepared by transfecting PLKO.1 shRNA plasmids and packaging plasmids containing pSPAX2 (Addgene, #12260) and pMD2.G (Addgene, #12259) into HEK293T cells using PEI (Polysciences) (See Supplemental Data 1 for oligo sequences). Collected conditional media containing virus particles were used to transduce cells in the growth media supplemented with Polybrene (Yeast) for 24 h. The infected cells were selected with 2 mg/ml puromycin for an extra 24 h. The cells were then switched into growth media without antibiotics and grown for an additional 24 h before being harvested for further analysis.

siRNAs were synthesized (Tsingke Biotech, Wuhan) and transfected with Lipofectamine RNAi-MAX (Life Technologies) in antibiotics-free medium according to the manufacturer's instructions. Cells were harvested 36 h after transfection with YAP/TAZ siRNAs and TAF4 siRNAs. The sequences of the primers are listed in Supplemental Data 1.

### Real-time qPCR and RNA-Sequencing

For RT-PCR, total RNA was isolated from cells with RNA Isolater Total RNA Extraction Reagent (RC112-01, Vazyme Biotech, Nanjing, China) according to the manufacturer's instructions. The isolated RNA was reverse transcribed into cDNA using HiScript II (Abclonal, #RK20428). Quantitative real-time PCR was performed with a CFX96™ Real-Time system (Bio-Rad, Hercules, CA) and SYBR Green PCR master mix (Abclonal, #RM21203). The fold change in the gene expression was calculated using the comparative Ct method, and three replicates were tested for each cDNA sample. *GAPDH* or *Gapdh* was used as an internal reference. The sequences of the primers are listed in Supplemental Data 1. Each experiment was repeated at least three times.

For RNA-sequencing, NCI-H1299 cells in 6-well plates were transfected with YAP/TAZ or TAF4 siRNAs at 50 nM for 48 h or treated with liposome delivered TJ-M11 at IC<sub>50</sub> value for 48 h. The scrambled siRNA or TJ-SV40 served as negative control. Total RNA was extracted from three biological replicates. RNA quality was assessed using a 2100 Expert Bioanalyzer (Agilent) and sent for library preparation and sequencing using the Illumina HiSeq2000 platform of BGI (Beijing, China). The data were analyzed on the free online BGI Dr.tom Platform.

### Immunofluorescence

The immunofluorescence experiments were performed as previously described. The cells were washed thrice with PBS, fixed with 4% paraformaldehyde (PFA) for 10 min, and permeabilized with 0.5% Triton X-100 for 15 min. Thereafter, the cells were washed with PBS and incubated with Image-iT signal enhancer (Thermo Fisher Scientific) for 30 min at room temperature. Subsequently, the cells were incubated with specific primary antibodies: YAP (Cell Signaling, #14074), Flag (Sigma, #F1804), HA (Cell Signaling, #3724), TTF-1 (ZSGB-Bio, #ZM-0270), E-cadherin (Invitrogen #13-1900) at 4 °C overnight. After washing with 0.1% Tween-20 (Sigma-Aldrich) in PBS four times, the cells were incubated for 1 h with secondary antibodies. Nuclei were counterstained with DAPI. Thereafter, the cells were rinsed with 0.1% Tween-20 in PBS four times and mounted with mounting medium. The coverslips were sealed with nail polish. The samples were scanned by the Olympus FV3000 confocal system.

### Generation of knockout cell lines with CRISPR-Cas9

*Yap* *TAD*<sup>+/−</sup>/*Taz*<sup>+/−</sup> and *MED15* knockout cells were created through the CRISPR-Cas9 system. Cells were transiently transfected with lenti-CRISPRv2 (Addgene, #52961) or pL-CRISPR.EFS.tRFP (Addgene, #57819). The guide sequences were designed using online tool the Optimized CRISPR Design (<https://www.atum.bio/cas9/input>). The guide sequences were listed in Supplemental Data 1. Following transfection and transient selection with puromycin for 3 days, the cells were diluted with medium (15 cells/ml) and plated into 96-well plates. Cells were allowed to grow for another 10 days. Knockout clones were selected by immunoblot analysis and genome sequencing.

### Cell viability and colony formation assay

Cell viability was evaluated by CCK8 assay, as previously described. Tumor cells were seeded into a 96-well microplate at a density of 4000 cells/well. At 60–70% confluence, the cells were treated with the indicated concentrations of the TJ-SV40 or TJ-M11 liposomes for 48 h, and then measure the cell viability. CCK8 solution (10  $\mu\text{L}$  of 2 mg/ml) was added to each well, incubating at 37 °C for 2 h. In order to determine the number of viable cells, the optical density (OD) of each well



was analyzed using an enzyme-linked immunosorbent assay plate reader (Bio-Tec) at a wavelength of 450 nm. The percentage of viable cells relative to the control was obtained as follows: Cell viability rate (%) = (OD value of treated group - background)/(OD value of control group - background) × 100. The determination of IC<sub>50</sub> values was conducted using GraphPad Prism.

For the colony formation experiment, cells were seeded at 2500 cells per well in 6-well plates and allowed to grow for one week. Colonies were stained using 0.1% crystal violet.

During liposomes-delivered peptides treatment assay, NCI-H1299 cells were seeded at 2000 cells per well in 6-well plates, when the cells attached, cells were washed with serum-free medium and treated with 5 μM TJ-M11 for 48 h. Then cells were switched to fresh complete medium, allowing to grow another 5 days. Colonies were stained using 0.1% crystal violet.

### RT-qPCR of nascent RNA

Total RNA was isolated from cells using the RNeasy Pure Kit (TIANGEN, DP430). After quantification using a Nanodrop spectrophotometer (Thermo Scientific), 500 ng of total RNA was reverse transcribed into cDNA using the cDNA Reverse Transcription Kit (ABclonal, RK20400) with oligo-d(T) as the reverse transcription primer. When quantifying nascent transcription, it is important to note that nascent RNAs are ectopic transcripts lacking splicing or polyadenylation<sup>61,62</sup>. We therefore used gene-specific primers for reverse transcription to synthesize nascent cDNA. For *CTGF*, we designed the reverse transcription primer at the first intron 87 nt from the TSS. 500 ng RNA, 10 mM dNTPs, specific primers (50 μM) and Nuclease-free H<sub>2</sub>O, denaturing the reaction system for 5 min at 65 °C, followed by the addition of the ABScript II reaction mix (2×) and the ABScript II enzyme mix (10×). ABScript II reaction mix (2×) and ABScript II enzyme mix (10×) were added for 1 h at 42 °C and the enzyme was finally inactivated at 80 °C for 5 min. The cDNA obtained was subjected to quantitative PCR using SYBR Green Real-Time PCR Master Mix (Vazyme). *GAPDH* was used as an internal control. The sequences of the PCR primers are given in Supplementary Data 1.

### CUT & Tag experiments

CUT&Tag assay was performed according to the standard protocol<sup>63</sup>. Briefly, NCI-H1299 cells were transfected with siNC or siYAP/TAZ and washed with ice-cold PBS twice. Then, 1 × 10<sup>5</sup> cells were washed with 1 ml of wash buffer (20 mM HEPES pH 7.5, 150 mM NaCl, 0.5 mM Spermidine (Vazyme, #TD903), 1× Protease inhibitor cocktail (Roche)) and centrifuged at 400 g for 5 min at room temperature. Cell pellets were resuspended with 100 μl of wash buffer. Concanavalin A-coated magnetic beads were washed twice with binding buffer (20 mM HEPES pH 7.5, 10 mM KCl, 1 mM MnCl<sub>2</sub>, 1 mM CaCl<sub>2</sub>). Next, 10 μl of activated beads were added and incubated at room temperature for 10 min. Bead-bound cells were resuspended in 50 μl of antibody buffer (20 mM HEPES pH 7.5, 150 mM NaCl, 0.5 mM Spermidine, 0.05% Digitonin, 2 mM EDTA, 0.1% BSA, 1× Protease inhibitor cocktail). Then, 3 μg of primary antibody (anti-RNA polymerase II CTD repeat YSPTSPS (Abcam, #ab817) or normal mouse IgG (Abclonal, #AC011) was added and incubated overnight at 4 °C with slow rotation. The primary antibody was removed using a magnet stand. Secondary antibody (1 μg) (Goat anti-Mouse IgG H&L (Abcam, #ab6708) was diluted in 50 μl of Dig-wash buffer (20 mM HEPES pH 7.5, 150 mM NaCl, 0.5 mM Spermidine, 0.05% Digitonin, 1× Protease inhibitor cocktail) and cells were incubated at room temperature for 1 h. Cells were washed three times with Dig-wash buffer to remove unbound antibodies. The hyperactive pA/G-TnP Transposase adapter complex (TTE mix, 2 μM) was diluted 1:50 in 100 μl of Dig-300 buffer (20 mM HEPES pH 7.5, 300 mM NaCl, 0.5 mM Spermidine, 0.01% Digitonin, 1× Protease inhibitor cocktail). Cells were incubated with 0.04 μM TTE mix at room temperature for

1 h. Cells were washed three times with 200 μl Dig-300 buffer to remove unbound TTE mix. Cells were then resuspended in 50 μl of Trueprep Tagment Buffer L (10 mM MgCl<sub>2</sub> in Dig-300 buffer) and incubated at 37 °C for 1 h. To terminate tagmentation and DNA purification, 5 μl Proteinase K, 100 μl Buffer L/B and 20 μl DNA Extract Beads were added to 50 μl of sample and incubated at 55 °C for 10 min. DNA were washed once with 200 μl Buffer WA, then washed twice with Buffer WB, and dissolved in 22 μl ddH<sub>2</sub>O.

For library amplification, 15 μl of DNA was mixed with 25 μl of 2× CUT&Tag Amplication Mix, as well as 5 μl of uniquely barcoded i5 and 5 μl i7 primers from TruePrep Index Kit V2 for Illumina (Vazyme, #TD202). A total volume of 50 μl of sample was placed in a Thermocycler using the following program: 72 °C for 3 min; 95 °C for 3 min; 17 cycles of 98 °C for 10 s, 60 °C for 5 s; 72 °C for 1 min and hold at 4 °C. To purify the PCR products, 1.6× volumes of VAHTS DNA Clean Beads (Vazyme) were added and incubated at room temperature for 5 min. Libraries were washed twice with 80% ethanol and eluted in 22 μl of ddH<sub>2</sub>O. Libraries were sequenced on an Illumina NovaSeq platform and 150-bp paired-end reads were generated.

All raw sequence data were quality trimmed to a minimum phred score of 20 using trimmomatic. Apparent PCR duplicates were removed using Picard MarkDuplicates v1.107. All reads produced by CUT&Tag of Pol II were aligned to the hg38 human genome using Bowtie2 version 2.3.5. Sequence tags were aligned to the genome and then subsequently analyzed by MACS2 software version 2.1.2 to detect genomic regions enriched for multiple overlapping DNA fragments (peaks) that we considered to be putative binding sites. Peaks with a false discovery rate lower than 5% were saved to detect chromosomal regions for further analysis. Visualization of peak distribution along genomic regions of interested genes was performed with IGV. Genes with a peak within 3 kb of the TSS were considered target genes.

### Mass spectrometry

The samples were subjected to a one-step process of protein denaturation, reduction, and alkylation by adding a reaction mixture (1% SDC, 100 mM Tris-HCl pH 8.5, 10 mM TCEP, 40 mM CAA) and incubating at 60 °C for 1 h. Following dilution with an equal volume of ultrapure water, trypsin was added at a 1:50 enzyme-to-protein ratio, and the enzymatic cleavage was carried out by overnight oscillation at 37 °C. On the following day, trypsin cleavage was terminated by adding TFA, and the supernatant was collected by centrifugation at 16,000 g. Desalting was performed using a self-made SDB column, and the eluate was lyophilized and stored at -20 °C for further use.

Mass spectrometric data were acquired using a Q Exactive Plus mass spectrometer coupled with an EASY-nLC 1200 liquid chromatography system. Peptide samples, dissolved in the loading buffer, were automatically injected and separated on an analytical column (C18, 2 μm, 100 Å). A 100-min gradient was established using two mobile phases (mobile phase A: 0.1% formic acid; mobile phase B: 0.1% formic acid, 80% ACN). The flow rate was set at 300 nl/min. Mass spectrometry was performed in DDA mode, with each scan cycle consisting of an MS full scan (R = 70 K, AGC = 3e6, max IT = 20 ms, scan range = 350–1800 m/z) and subsequent 15 MS/MS scans (R = 17.5 K, AGC = 2e5, max IT = 50 ms). HCD collision energy was set at 28, and the isolation window for the quadrupole was set to 1.6 Da. The dynamic exclusion time for repeated ion acquisition was set to 35 s.

Mass spectrometry data were processed using MaxQuant (V1.6.6) software with the Andromeda database search algorithm. The Uniport Human protein database was employed for database searching. The results were filtered with 1% FDR at the protein and peptide levels, excluding reverse database proteins, contaminant proteins, and proteins with only one modified peptide segment. The remaining identification information was used for subsequent analysis.



## Plasmid constructions

For recombinant protein purification, human YAP-TAD, YAP, and YAP-mEGFP were inserted into pET22b vector fusion with 6×His-tag at the N terminus. Human MED15-ABD1, ABD2, ABD3, YAP-CC, TAF4 M1, TAFH, and TAF4<sub>582-837</sub> were inserted into pET30a plasmid fusion with 6×His-tag or 6×His-SUMO-tag at the N terminus. The full length of human MED15 (isoform2), YAP and TAZ were inserted into pFAST bacmid with 8×His-tag at the N terminus.

## Sf9 cell culture

The pFastBac plasmid and DH10Bac *E. coli* (Weidibio) were used to create recombinant bacmids. The bacmid was transfected into Sf9 cells (Expression Systems) with FuGENE® HD Transfection Reagent to generate recombinant baculovirus. The human-derived MED15, YAP, TAZ bacmids were transfected into Sf9 cells using FuGENE® HD Transfection Reagent (Expression Systems). Recombinant baculovirus was amplified 3 times in Sf9 cells. 20 ml of the 3<sup>rd</sup> amplification solution was used to infect 1 l of Sf9 cells (Expression Systems) at a rate of  $1 \times 10^6$  cells/ml and incubated at 27 °C for 72 h. Cells were harvested by centrifugation at 1500 g.

## Protein expression and purification

Human YAP, YAP-mEGFP and the human YAP-TAD were expressed in *E. coli* BL21(DE3). Expression of proteins was induced by addition of 1 mM or 0.4 mM IPTG at 18 °C for 18 h. Extracts were prepared with buffer A (50 mM HEPES pH 7.5, 200 mM NaCl, 2 mM TCEP, 20 mM imidazole), followed by chromatography with Ni-NTA resin (Qiagen, 30210) and eluted with an imidazole gradient (Sigma, 792527). Human YAP, YAP-mEGFP were further purified by gel-filtration on a Hiload 16/600 200 pg (GE28-9893-35). The protein was concentrated and dispensed in the storage buffer (20 mM Tris-HCl, pH 7.5, 150 mM NaCl, 2 mM TCEP) after quantification with the Nanodrop 2000 (Thermo Scientific, 23225). Proteins were finally stored at -80 °C before use. The full length of human MED15(1-748), YAP and TAZ were transformed in insect cell. After culturing at 27 °C for 72 h, cells were harvested by centrifugation at 1500 rpm for 10 min. Then the cells were extracted with lysis buffer (50 mM HEPES pH 8.0, 300 mM NaCl, 5 mM MgCl<sub>2</sub>, 2 mM TCEP, 30 mM imidazole, 10% glycerol, 1 mM PMSF supplemented with protease inhibitor cocktail). The crude extracts were further clarified by centrifugation at 18,000 rpm for 30 min with R10A5-1520 rotor (Himac). The supernatant was loaded onto affinity chromatography with Ni-NTA beads, washed with binding buffer including 0.05% CHAPS, 5 mM ATP (no protease inhibitors) and eluted with an imidazole gradient (Sigma, catalog no. 792527). Peak fractions were collected, concentrated, quantified and further purified by gel-filtration on a Hiload 16/600 200 pg (GE28-9893-35). Fractions containing His-MED15 were concentrated to -1 mg/ml and flash-frozen in liquid nitrogen or used for subsequent analysis.

## Protein CY3 labeling

The purified protein was diluted in 20 mM HEPES, 150 mM NaCl, 2 mM TCEP (pH 7.5) and mixed with Cy3 (MCE, HY-D0822) at a molar ratio of 1:10. The mixture was reacted on a shaker overnight at 4 °C. Additional fluorescent dye is removed through a PD-10 column (GE17-0853-02). Labeled proteins were concentrated using an Amicon Ultra-15 centrifugal filter device (Millipore) and stored in His-MED15 storage buffer (20 mM Tris, pH 7.5, 150 mM NaCl).

## Liquid droplet formation

His-MED15-CY3 and His-YAP-mEGFP were both stored in a buffer containing 20 mM Tris pH 7.5, 150 mM NaCl and pre-cleared via high-speed centrifugations. Typically, the two proteins were mixed at final concentrations spanning 2.5–40 μM, with 10% PEG. For imaging, droplets were observed either in solution drops by light microscope or by injecting mixtures into a homemade flow chamber comprised of a

glass slide sandwiched by a coverslip with one layer of double-sided tape as a spacer for DIC (Olympus FV300) or fluorescence imaging (Olympus FV300).

## Chemical synthesis of linear peptides

The linear peptides were manually synthesized by carrying out standard Fmoc-based peptide syntheses using 2-Chlorotriyl Chloride resin. (1) Deprotection: Remove DMF, add 20% piperidine DMF solution (15 ml/g), 5 min, remove and add 20% piperidine DMF solution (15 ml/g), 15 min. The resin was washed with DMF (10 ml/g) twice, methanol (10 ml/g) twice, DMF (10 ml/g) twice. (2) Condensation: Add 3 times molar excess of Fmoc protected amino acids, 3 times molar excess of HBTU, then 10 times molar excess of DIEA, finally add DMF to dissolve and shake for 45 min. The resin was washed with DMF (10 ml/g) once, methanol (10 ml/g) twice, DMF (10 ml/g) twice. (3) Wash the resin and pump dry: DMF (10 ml/g) twice, DCM (10 ml/g) three times, methanol (10 ml/g) four times and pump dry for 10 min. (4) TFA cleavage: Preparation of cutting solution (10 ml/g) TFA 95%; water 2%; EDT 2%; TIS 1%, 180 min. (5) Blow-dry washing: The lysate is blown as dry as possible with nitrogen, ether is precipitated. The supernatant is removed by centrifugation, and the precipitate is washed six times with ether and then evaporated at room temperature.

The product was dissolved in a H<sub>2</sub>O/ACN, purified using HPLC, analyzed using ESI-MS, and dried using a lyophilizer to afford a white powder. To facilitate monitoring of the distribution of the peptide in some assays, a fluorescent FITC moiety was chemically attached to the N-terminus of the peptide.

## NMR sample preparation

TADs of human YAP/TAZ, ABD1-3 of MED15, YAP-CC, TAF4-M1, TAF4<sub>582-837</sub>, TAF4-M2, and TAFH were expressed in *E. coli* BL21(DE3). Expression of proteins was induced by the addition of 1 mM or 0.2 mM IPTG at 18 °C for 18 h. TADs of YAP/TAZ, ABD1-3 of MED15, TAF4M1, and TAF4<sub>582-837</sub> were cloned into a pET22a or pET30a vector. Bacteria are expressed in M9 minimal medium supplemented with <sup>15</sup>NH<sub>4</sub>Cl and/or <sup>13</sup>C-glucose to gain uniformly <sup>15</sup>N- or <sup>13</sup>C/<sup>15</sup>N-labeled proteins. At OD<sub>600</sub> nm of 0.8, protein expression is induced by the addition of 0.4 mM IPTG for 16 h at 18 °C. Bacteria are harvested by centrifugation, suspended in 50 mM HEPES, pH 7.5, 200 mM NaCl, 2 mM TCEP, 20 mM imidazole, buffer containing protease inhibitors (Protease Inhibitor Cocktail, Bacteria) and disrupted by a high-pressure homogenizer. The extract is centrifuged at 18,000 g for 35 min. Tagged proteins are purified by affinity chromatography using HisTrap (GE Healthcare) and a last step of size-exclusion chromatography using a Superdex75 increase 10/300 pg (GE Healthcare).

## Hydrogen-deuterium exchange (HDX) detected by mass spectrometry (MS)

Peptides were identified using tandem MS (MS/MS) with a Fusion Orbitrap mass spectrometer (Thermo Fisher Scientific). Product ion spectra were acquired in data-dependent mode with the top eight most abundant ions selected for the product ion analysis per scan event. The MS/MS data files were submitted to Proteome Discover 2.4 (Thermo Fisher Scientific) for high-confident peptide identification.

8 μM of the apo His-MED15 protein was mixed with 1:2 molar excess of His-YAP and incubated for 30 min at 4 °C for complex formation before subjecting them to HDX analysis. Five-microliter of protein/protein complex with ligand/peptide was diluted into 16 ml D<sub>2</sub>O on exchange buffer (50 mM HEPES, pH 7.5, 50 mM NaCl, 2 mM DTT) and incubated for various HDX time points (e.g., 0, 10, 60, 300 s) at 4 °C and quenched by mixing with 20 ml of ice-cold 3 M HCl, 1% trifluoroacetic acid.

Each quenched sample was immediately injected into the LEAP Pal 3.0 HDX platform. Upon injection, samples were passed through an immobilized pepsin column (2 mm × 2 cm) at 120 μl/min and the

digested peptides were captured on a C18 PepMap300 trap column (Thermo Fisher Scientific) and desalted. Peptides were separated across a 2.1 mm × 5 cm C18 column (1.9 μm Hypersil Gold, Thermo Fisher Scientific) with a linear gradient of 4–40% CH<sub>3</sub>CN and 0.3% formic acid, over 6 min. Sample handling, protein digestion, and peptide separation were conducted at 4 °C. Mass spectrometric data were acquired using a Fusion Orbitrap mass spectrometer (Thermo Fisher Scientific) with a measured resolving power of 65,000 at m/z 400. HDX analysis were performed in triplicate, with single preparations of each protein ligand complex. The intensity weighted mean m/z centroid value of each peptide envelope was calculated and subsequently converted into a percentage of deuterium incorporation. Statistical significance for the differential HDX data is determined by an unpaired t test for each time point, a procedure that is integrated into the HDX Workbench software. Corrections for back-exchange were made on the basis of an estimated 70% deuterium recovery, and accounting for the known 80% deuterium content of the deuterium exchange buffer.

The HDX data from all overlapping peptides were consolidated to individual amino acid values using a residue averaging approach. Briefly, for each residue, the deuterium incorporation values and peptide lengths from all overlapping peptides were assembled. Deuterium incorporation values were then weighted by the inverse of the peptide length. Each of the weighted deuterium incorporation values was then averaged to produce a single value for each amino acid. The initial two residues of each peptide, as well as prolines, were omitted from the calculations.

### Statistics analysis

All data are presented as the mean ± SEM. Statistical analysis was performed using GraphPad Prism 7.0 software. Significant differences were assessed by 2-tailed unpaired Student's t test or 1-way or 2-way ANOVA statistical analyses. GSEA analysis was performed using GSEA software. KEGG pathway enrichment analysis was performed using DAVID. The statistical parameters are present in the figures and figure legends. Significance was set as  $P < 0.05$ .

### Study approval

IRB approval was obtained for use of human tissues (Medical Ethics Committee of Tongji Hospital, Huazhong University of Science and Technology TJ-IRB20230922), which were collected with written informed consent. All animal procedures were performed in accordance with Medical Ethics Committee of Tongji Medical College, Huazhong University of Science and Technology.

### Reporting summary

Further information on research design is available in the Nature Portfolio Reporting Summary linked to this article.

### Data availability

The RNA-Seq and CUT&Tag data have been submitted to the NCBI repository SRA (Bioproject accession number: PRJNA967199). The BioID mass spectrometry data are available via ProteomeXchange with identifier PXD053795 and PXD060955. The NMR structures of MED15-ABD3 and YAP-TAD have been uploaded to the PDB database (PDB ID: 8J9A; PDB ID: 8WRG). NMR-related data for YAP/TAZ-TAD, MED15-ABD3 and TAFH have been uploaded to Biological Magnetic Resonance Bank (BMRB) with BMRB IDs 51948, 51947, 36565, and 51945, respectively. The remaining data are available within the Article, Supplementary Information or Source Data file. PRJNA967199: <https://www.ncbi.nlm.nih.gov/bioproject/PRJNA967199/>; PXD053795: <https://www.ebi.ac.uk/pride/archive?keyword=PX053795>; PXD060955: <https://www.ebi.ac.uk/pride/archive?keyword=PX060955>. Source data are provided with this paper.

## References

- Zanconato, F., Cordenonsi, M. & Piccolo, S. YAP/TAZ at the roots of cancer. *Cancer Cell* **29**, 783–803 (2016).
- Zheng, Y. & Pan, D. The hippo signaling pathway in development and disease. *Dev. Cell* **50**, 264–282 (2019).
- Ibar, C. & Irvine, K. D. Integration of Hippo-YAP signaling with metabolism. *Dev. Cell* **54**, 256–267 (2020).
- Hansen, C. G., Moroishi, T. & Guan, K. L. YAP and TAZ: a nexus for Hippo signaling and beyond. *Trends Cell Biol.* **25**, 499–513 (2015).
- Johnson, R. & Halder, G. The two faces of Hippo: targeting the Hippo pathway for regenerative medicine and cancer treatment. *Nat. Rev. Drug Discov.* **13**, 63–79 (2014).
- Ni, X. et al. YAP is essential for treg-mediated suppression of anti-tumor immunity. *Cancer Discov.* **8**, 1026–1043 (2018).
- Bhandoola, A. et al. Yap suppresses T-cell function and infiltration in the tumor microenvironment. *PLOS Biol.* **18**, e3000591 (2020).
- Wu, B.-K., Mei, S.-C., Chen, E. H., Zheng, Y. & Pan D. YAP induces an oncogenic transcriptional program through TET1-mediated epigenetic remodeling in liver growth and tumorigenesis. *Nat. Genet.* **58**, 1202–1213 (2022).
- Cordenonsi, M. & Piccolo, S. Transcriptional addiction in cancer cells is mediated by YAP/TAZ through BRD4. *Nat. Med.* **24**, 1599–1610 (2018).
- Chang, L. et al. The SWI/SNF complex is a mechanoregulated inhibitor of YAP and TAZ. *Nature* **563**, 265–269 (2018).
- Skibinski, A. et al. The hippo transducer TAZ interacts with the SWI/SNF complex to regulate breast epithelial lineage commitment. *Cell Rep.* **6**, 1059–1072 (2014).
- Ferrie, J. J., Karr, J. P., Tjian, R. & Darzacq, X. “Structure”-function relationships in eukaryotic transcription factors: The role of intrinsically disordered regions in gene regulation. *Mol. Cell* **82**, 3970–3984 (2022).
- DelRosso, N. et al. Large-scale mapping and mutagenesis of human transcriptional effector domains. *Nature* **616**, 365–372 (2023).
- Arnold, C. D. et al. A high-throughput method to identify trans-activation domains within transcription factor sequences. *EMBO J.* **37**, e98896 (2018).
- Erijman, A. et al. A high-throughput screen for transcription activation domains reveals their sequence features and permits prediction by deep learning. *Mol. Cell* **78**, 890–902.e896 (2020).
- Kapoor, A. et al. Yap1 activation enables bypass of oncogenic KRAS addiction in pancreatic cancer. *Cell* **158**, 185–197 (2014).
- Moya, I. M. & Halder, G. Hippo-YAP/TAZ signalling in organ regeneration and regenerative medicine. *Nat. Rev. Mol. Cell Biol.* **20**, 211–226 (2019).
- Liu-Chittenden, Y. et al. Genetic and pharmacological disruption of the TEAD-YAP complex suppresses the oncogenic activity of YAP. *Genes Dev.* **26**, 1300–1305 (2012).
- Maity, S., Gridnev, A. & Misra, J. R. Assays used for discovering small molecule inhibitors of YAP activity in cancers. *Cancers* **14**, 1029 (2022).
- Jiao, S. et al. A peptide mimicking VGLL4 function acts as a YAP antagonist therapy against gastric cancer. *Cancer Cell* **25**, 166–180 (2014).
- Allen, B. L. et al. Suppression of p53 response by targeting p53-Mediator binding with a stapled peptide. *Cell Rep.* **39**, 110630 (2022).
- Xu, Y. et al. A TFIID-SAGA perturbation that targets MYB and suppresses acute myeloid leukemia. *Cancer Cell* **33**, 13–28.e18 (2018).
- Bushweller, J. H. Targeting transcription factors in cancer - from undruggable to reality. *Nat. Rev. Cancer* **19**, 611–624 (2019).
- Yu, M. et al. Interferon-γ induces tumor resistance to anti-PD-1 immunotherapy by promoting YAP phase separation. *Mol. Cell* **81**, 1216–1230.e1219 (2021).

25. Oka, T. & Sudol, M. Nuclear localization and pro-apoptotic signaling of YAP2 require intact PDZ-binding motif. *Genes Cells* **14**, 607–615 (2009).
26. Peng, Z. et al. Protocol to establish a lung adenocarcinoma immunotherapy allograft mouse model with FACS and immunofluorescence-based analysis of tumor response. *STAR Protoc.* **2**, 100595 (2021).
27. Christofides, A. et al. The complex role of tumor-infiltrating macrophages. *Nat. Immunol.* **23**, 1148–1156 (2022).
28. Guo, X. et al. Single tumor-initiating cells evade immune clearance by recruiting type II macrophages. *Genes Dev.* **31**, 247–259 (2017).
29. Taniguchi, S. et al. Tumor-initiating cells establish an IL-33–TGF- $\beta$  niche signaling loop to promote cancer progression. *Science* **369**, eaay1813 (2020).
30. Wang, X. et al. Conserved region I of human coactivator TAF4 binds to a short hydrophobic motif present in transcriptional regulators. *Proc. Natl. Acad. Sci. USA* **104**, 7839–7844 (2007).
31. Galli, G. G. et al. YAP drives growth by controlling transcriptional pause release from dynamic enhancers. *Mol. Cell* **60**, 328–337 (2015).
32. Hou, L. et al. Paf1C regulates RNA polymerase II progression by modulating elongation rate. *Proc. Natl. Acad. Sci.* **116**, 14583–14592 (2019).
33. Cai, D. et al. Phase separation of YAP reorganizes genome topology for long-term YAP target gene expression. **21**, 1578–1589 (2019).
34. Franklin, J. M. & Guan, K. L. YAP/TAZ phase separation for transcription. *Nat. Cell Biol.* **22**, 357–358 (2020).
35. Lu, Y. et al. Phase separation of TAZ compartmentalizes the transcription machinery to promote gene expression. *Nat. Cell Biol.* **22**, 453–464 (2020).
36. Tuttle, L. M. et al. Gcn4-mediator specificity is mediated by a large and dynamic fuzzy protein-protein complex. *Cell Rep.* **22**, 3251–3264 (2018).
37. Brzovic, P. S. et al. The acidic transcription activator Gcn4 binds the mediator subunit Gal11/Med15 using a simple protein interface forming a fuzzy complex. *Mol. Cell* **44**, 942–953 (2011).
38. Ma, L. et al. Co-condensation between transcription factor and coactivator p300 modulates transcriptional bursting kinetics. *Mol. Cell* **81**, 1682–1697.e1687 (2021).
39. Wu, Z. et al. YAP silencing by RB1 mutation is essential for small-cell lung cancer metastasis. *Nat. Commun.* **14**, 5916 (2023).
40. LeSavage, B. L., Suhar, R. A., Brogiere, N. & Lutolf, M. P. Next-generation cancer organoids. *Nat. Mater.* **21**, 143–159 (2022).
41. Yu, M. et al. Interferon- $\gamma$  induces tumor resistance to anti-PD-1 immunotherapy by promoting YAP phase separation. *Mol. Cell* **81**, 1216–1230.e1219 (2021).
42. Battilana, G., Zanonato, F. & Piccolo, S. Mechanisms of YAP/TAZ transcriptional control. *Cell Stress* **5**, 167–172 (2021).
43. Malik, S. & Roeder, R. G. The metazoan Mediator co-activator complex as an integrative hub for transcriptional regulation. *Nat. Rev. Genet.* **11**, 761–772 (2010).
44. Dey, A., Varelas, X. & Guan, K. L. Targeting the Hippo pathway in cancer, fibrosis, wound healing and regenerative medicine. *Nat. Rev. Drug Discov.* **19**, 480–494 (2020).
45. Zanonato, F. et al. Transcriptional addiction in cancer cells is mediated by YAP/TAZ through BRD4. *Nat. Med.* **24**, 1599–1610 (2018).
46. Cho, Y. S. et al. CDK7 regulates organ size and tumor growth by safeguarding the Hippo pathway effector Yki/Yap/Taz in the nucleus. *Genes Dev.* **34**, 53–71 (2020).
47. Yagi, R., Chen, L. F., Shigesada, K., Murakami, Y. & Ito, Y. A WW domain-containing yes-associated protein (YAP) is a novel transcriptional co-activator. *Embo J.* **18**, 2551–2562 (1999).
48. Chong, S. et al. Tuning levels of low-complexity domain interactions to modulate endogenous oncogenic transcription. *Mol. Cell* **82**, 2084–2097.e2085 (2022).
49. Zamudio, A. V. et al. Mediator condensates localize signaling factors to key cell identity genes. *Mol. Cell* **76**, 753–766.e756 (2019).
50. Boija, A. et al. Transcription factors activate genes through the phase-separation capacity of their activation domains. *Cell* **175**, 1842–1855.e1816 (2018).
51. McSwiggen, D. T. et al. Evidence for DNA-mediated nuclear compartmentalization distinct from phase separation. *eLife* **8**, e47098 (2019).
52. Trojanowski, J. et al. Transcription activation is enhanced by multivalent interactions independent of phase separation. *Mol. Cell* **82**, 1878–1893.e1810 (2022).
53. Roux, K. J., Kim, D. I., Raida, M. & Burke, B. A promiscuous biotin ligase fusion protein identifies proximal and interacting proteins in mammalian cells. *J. Cell Biol.* **196**, 801–810 (2012).
54. Gupta, G. D. et al. A dynamic protein interaction landscape of the human centrosome-cilium interface. *Cell* **163**, 1484–1499 (2015).
55. Driehuis, E., Kretschmar, K. & Clevers, H. Establishment of patient-derived cancer organoids for drug-screening applications. *Nat. Protoc.* **15**, 3380–3409 (2020).
56. Rieping, W. et al. ARIA2: automated NOE assignment and data integration in NMR structure calculation. *Bioinformatics* **23**, 381–382 (2006).
57. Delaglio, F. et al. NMRPipe: a multidimensional spectral processing system based on UNIX pipes. *J. Biomol. NMR* **6**, 277–293 (1995).
58. Lee, W., Rahimi, M., Lee, Y. & Chiu, A. POKY: a software suite for multidimensional NMR and 3D structure calculation of biomolecules. *Bioinformatics* **37**, 3041–3042 (2021).
59. Shen, Y. & Bax, A. Protein backbone and sidechain torsion angles predicted from NMR chemical shifts using artificial neural networks. *J. Biomol. NMR* **56**, 227–241 (2013).
60. Laskowski, R. A., MacArthur, M. W., Moss, D. S. & Thornton, J. M. PROCHECK: a program to check the stereochemical quality of protein structures. *J. Appl. Crystallogr.* **26**, 283–291 (1993).
61. Core, L. J., Waterfall, J. J. & Lis, J. T. Nascent RNA sequencing reveals widespread pausing and divergent initiation at human promoters. *Science* **322**, 1845–1848 (2008).
62. Roberts, T. C. et al. Quantification of nascent transcription by bromouridine immunocapture nuclear run-on RT-qPCR. *Nat. Protoc.* **10**, 1198–1211 (2015).
63. Wu, S. J. et al. Single-cell CUT&Tag analysis of chromatin modifications in differentiation and tumor progression. *Nat. Biotechnol.* **39**, 819–824 (2021).

## Acknowledgements

We thank Kenneth Irvine, Bing Zhao, and Dawang Zhou for sharing reagents and discussion of the manuscript writing. We appreciate the help from Gilsai biotech (Nanning, China) for the SPR experiments. This research was supported by Ministry of Science and Technology of China (2020YFA0803201) and National Natural Science Foundation of China (82430095, 32270762, and 82002972). We thank the Laboratory Animal Center of Huazhong University of Science and Technology for providing the mouse culture support.

## Author contributions

M.Y. and J.W. performed the experiments and analyzed the data, respectively, and both authors contributed equally to the publication. X.Z. helped the mouse experiments; H.Z. helped the NMR data analysis. C.L. and J.Z. contributed to HDX experiments; J.Li., J.Lin., and L.H. contributed to human sample collection; S.S. and Y.L. contributed experimental design, data analysis, and manuscript preparation.

## Competing interests

The authors have declared that no conflict of interest exists. Y.L., S.S., J.Q., and N.Q. have filed patents (202310492752.3 and 202310893961.9) for the peptide inhibitors in China.

## Additional information

**Supplementary information** The online version contains supplementary material available at <https://doi.org/10.1038/s41467-025-59309-w>.

**Correspondence** and requests for materials should be addressed to Yan Li or Shuguo Sun.

**Peer review information** *Nature Communications* thanks the anonymous reviewer(s) for their contribution to the peer review of this work. A peer review file is available.

**Reprints and permissions information** is available at <http://www.nature.com/reprints>

**Publisher's note** Springer Nature remains neutral with regard to jurisdictional claims in published maps and institutional affiliations.

**Open Access** This article is licensed under a Creative Commons Attribution-NonCommercial-NoDerivatives 4.0 International License, which permits any non-commercial use, sharing, distribution and reproduction in any medium or format, as long as you give appropriate credit to the original author(s) and the source, provide a link to the Creative Commons licence, and indicate if you modified the licensed material. You do not have permission under this licence to share adapted material derived from this article or parts of it. The images or other third party material in this article are included in the article's Creative Commons licence, unless indicated otherwise in a credit line to the material. If material is not included in the article's Creative Commons licence and your intended use is not permitted by statutory regulation or exceeds the permitted use, you will need to obtain permission directly from the copyright holder. To view a copy of this licence, visit <http://creativecommons.org/licenses/by-nc-nd/4.0/>.

© The Author(s) 2025